materials

MDPI

Review

Chemoresistive Gas Sensors Based on Noble-Metal-Decorated Metal Oxide Semiconductors for H_2 Detection

Min Zhu, Heng Zhang, Shengming Zhang, Haiyu Yao, Xuerong Shi * and Shusheng Xu *

School of Material Science and Engineering, Shanghai University of Engineering Science, Shanghai 201620, China; m350123105@sues.edu.cn (M.Z.); m355124217@sues.edu.cn (H.Z.); m355123203@sues.edu.cn (S.Z.); m350122116@sues.edu.cn (H.Y.)

* Correspondence: shixuer05@mails.ucas.ac.cn (X.S.); xushusheng@sues.edu.cn (S.X.)

Abstract: Hydrogen has emerged as a prominent candidate for future energy sources, garnering considerable attention. Given its explosive nature, the efficient detection of hydrogen (H_2) in the environment using H_2 sensors is paramount. Chemoresistive H_2 sensors, particularly those based on noble-metal-decorated metal oxide semiconductors (MOSs), have been extensively researched owing to their high responsiveness, low detection limits, and other favorable characteristics. Despite numerous recent studies and reviews reporting advancements in this field, a comprehensive review focusing on the rational design of sensing materials to enhance the overall performance of chemoresistive H_2 sensors based on noble-metal-decorated MOFs is lacking. This review aims to address this gap by examining the principles, applications, and challenges of chemoresistive H_2 sensors, with a specific focus on Pd-decorated and Pt-decorated MOSs-based sensing materials. The observations and explanations of strategies employed in the literature, particularly within the last three years, have been analyzed to provide insights into the latest research directions and developments in this domain. This understanding is essential for designing and fabricating highly efficient H_2 sensors.

Keywords: noble metal; metal oxide semiconductors; chemoresistive; H_2 sensors

Academic Editor: Albena Paskaleva

Received: 18 December 2024
Revised: 14 January 2025
Accepted: 16 January 2025
Published: 19 January 2025

Citation: Zhu, M.; Zhang, H.; Zhang, S.; Yao, H.; Shi, X.; Xu, S. Chemoresistive Gas Sensors Based on Noble-Metal-Decorated Metal Oxide Semiconductors for H_2 Detection. *Materials* **2025**, *18*, 451. https://doi.org/10.3390/ma18020451

1. Introduction

Hydrogen(H_2), serving as both a reducing and carrier gas and a novel energy source, holds immense application value in the chemical, electronics, healthcare, and metal smelting industries. However, H_2 is susceptible to leakage during its production, storage, transportation, and utilization processes. H_2 is undetectable by smell due to its lack of color and odor, and high concentrations can cause asphyxiation. Furthermore, when its volumetric concentration in the air falls within the range of 4% to 75%, H_2 becomes susceptible to explosion upon exposure to an open flame. Consequently, the deployment of H_2 sensors for detecting H_2 content in the environment and monitoring its leakage during usage is imperative. Despite advancements in the development of various H_2 sensors, real-time leak detection and precise localization of leak sources remains challenging due to the fast diffusion of H_2 [1–5].

An excellent gas sensor should exhibit high responsiveness, fast response/recovery times, robust stability, and exceptional selectivity [6]. Fast response and recovery times for H_2 detection are essential to achieve real-time monitoring [7]. A low detection limit is also required. For instance, medical diagnosis necessitates a reliable H_2 gas sensor with a detection limit of approximately 10 ppm to aid healthcare providers in diagnosing specific digestive issues [8].

To develop a highly efficient H_2 sensor, extensive research efforts have been undertaken and subsequently summarized. Kafil et al. [9] directed their attention towards specific sensor parameters, including sensitivity, selectivity, humidity tolerance, and response time, among others, and proposed corresponding enhancement strategies while analyzing the underlying causes. Sharma et al. [10] concentrated on recent advancements in metal oxide semiconductor (MOS)-based and field effect transistor (FET)-based H_2 sensors, discussing the pertinent sensing techniques, mechanisms, and factors influencing sensor sensitivity. Kamal Hossain et al. [11] summarized strategies to augment H_2 sensing performances using noble-metal-decorated nanostructured zinc oxide (ZnO) as sensing materials. Despite the plethora of recent research endeavors and reviews reporting advancements in this field, a comprehensive review specifically focusing on the rational design of sensing materials to enhance the overall performance of chemoresistive H_2 sensors based on noble-metal-decorated MOSs remains elusive. Herein, we compile observations and explanations of strategies employed in the literature, particularly within the last three years, to provide insights into the latest research directions and developments in this domain. Initially, it introduces the classifications and fundamental operational principles of H_2 sensors. Following this introduction, the review delves into a comprehensive analysis of the specific operational mechanisms of chemoresistive MOSs-based H_2 sensors, employing illustrative examples to elucidate these mechanisms. The third section of this review explores the recent progress in the utilization of noble-metal-decorated MOSs for the development of high-performance H_2 sensors. Ultimately, the review concludes with a concise summation and delineates potential avenues for future research and development.

Types and Working Principles

H_2 sensors are primarily categorized into the subsequent classifications (Figure 1).

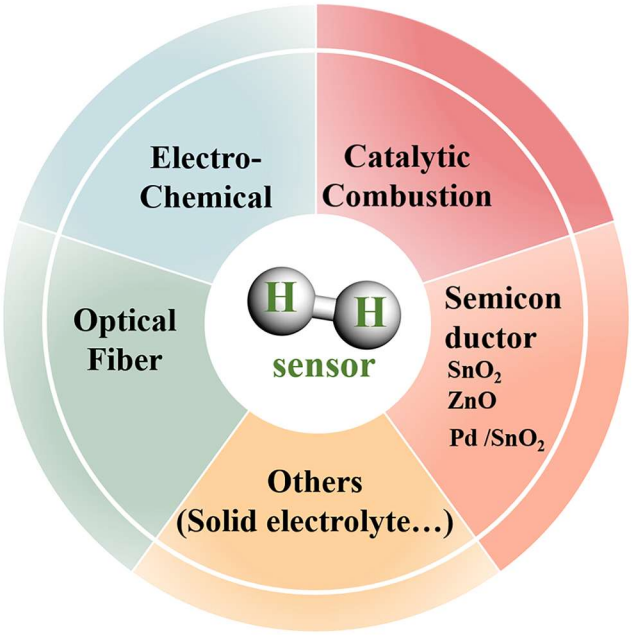

Figure 1. Classification of H_2 sensors.

(1) Electrochemical H_2 Sensor

An electrochemical H_2 sensor functions through the utilization of electrochemical reactions. The interaction of H_2 with the surface of the working electrode elicits variations in the potential of the electrode or adjustments in the circuit current. These modifications can be meticulously measured through the utilization of a reference electrode for calibra-

tion, thereby facilitating the precise detection of H_2 concentration fluctuations. LaConti et al. [12] innovatively deployed a specialized electrochemical sensor in 1971 for the quantitative determination of H_2 concentrations in gas mixtures containing electrochemically inactive species. After this work, electrochemical H_2 sensors have undergone significant advancements. In a recent contribution, Wang et al. [13] deliberated on the progression of solid-state electrochemical H_2 sensors.

(2) Catalytic Combustion H_2 Sensors

H_2, characterized as a combustible gas, undergoes a rapid oxidation reaction with oxygen (O_2), leading to the release of heat. This thermal signal is subsequently converted into an electrical signal via a sensitive transducer element. Depending on the methodology employed for converting thermal signals into electrical signals, these sensors can be further categorized into Pellistor and thermoelectric H_2 gas sensors. The operational principle of the Pellistor H_2 sensor involves the generation of heat through a chemical reaction, causing an elevation in temperature of the temperature-sensitive material. This temperature change results in a variation in resistance and, consequently, the creation of a potential difference. In contrast, thermoelectric H_2 sensors generate electrical signals through the utilization of the thermoelectric effect, also known as the Seebeck effect. In 1985, J.F. McAleer and his colleagues introduced the concept of the thermoelectric H_2 sensor, thereby laying the theoretical groundwork for subsequent investigative endeavors in the field of thermoelectric H_2 sensing technologies [14]. More recently, Zhang et al. [15] developed a new catalytic combustion H_2 sensor using the electrodeposition method.

(3) Optical fiber H_2 sensors

Optical H_2 sensors operate by detecting changes in the optical properties of a material upon exposure to H_2. The utilization of optical fibers as sensing elements in H_2 sensors was first reported by Butler et al. in the 1980s. The primary advantages of optical fiber H_2 sensors include their corrosion resistance, suitability for remote sensing, and resistance to electromagnetic interference [16]. Shen et al. [17] has summarized various optical fiber H_2 sensing technologies since 1984.

(4) Semiconductor-type sensors

This type of H_2 sensor primarily operates on the basis of the chemical interaction between H_2 and sensitive materials, which can be readily transduced into an electro-optical signal capable of quantitative assessment. In 1962, Seiyama and colleagues were the first to utilize the unique properties of semiconductor materials for the development of gas sensors [18]. They fabricated gas sensors utilizing zinc oxide (ZnO) semiconductor materials and observed the change of the sensor's resistance when exposed to reducing gases.

Over the past few years, advancements in material synthesis techniques and the iterative refinement of processing technologies have facilitated the development of high-performance H_2 sensors. Among them, MOS-based H_2 sensors boast numerous advantages, including rapid response times, cost-effectiveness, and ease of integration, leading to their extensive application. Various techniques for synthesizing MOSs have been reported, including gas-liquid-solid (GLS) technology [19], electrospinning [20], sol-gel processing [21], hydrothermal synthesis [22], and carbon-thermal transport growth [23]. GLS is commonly used for nanowires, but has complex procedures. Electrospinning is efficient for one-dimensional (1D) nanostructures, but may use toxic solvents. The sol-gel method allows for homogeneous mixing, but may leave residual pores and carbon, requiring heat treatment. Hydrothermal synthesis suits a range of microstructures, but requires precise control. Carbon-thermal transport growth offers specific morphologies and sizes, but may compromise stability and reproducibility. Various MOSs are commonly employed in gas sensing, such as ZnO and tin oxide (SnO_2), among others.

However, the poor electronic conductivity of MOSs constrains electron transport during gas–solid interactions, and MOSs usually exhibit limited activity for H_2 detection. To enhance the gas-sensing performance of MOS-based materials, various strategies have been employed, including morphology and size adjustment, exposure of high-energy crystal planes, structural modification, and noble metal decoration. Among these strategies, noble metal decoration was widely employed.

In recent years, considerable research has been conducted on noble-metal-decorated MOS H_2 sensors. As illustrated in Figure 2, over the past decade, the majority of studies on noble metals have concentrated on Palladium (Pd), Platinum (Pt), Gold (Au), Iridium (Ir), and Silver (Ag) for modifying MOSs-based H_2 sensors. Meanwhile, research on MOSs has primarily focused on n-type semiconductors such as SnO_2, ZnO, Titanium dioxide (TiO_2), and tungsten trioxide (WO_3), as well as p-type MOSs like nickel oxide (NiO), copper oxide (CuO), and Tricobalt tetraoxide (Co_3O_4). Numerous studies have demonstrated that the chemical/electronic sensitization of noble metals can substantially enhance the response and selectivity of sensors towards specific gases [24–26].

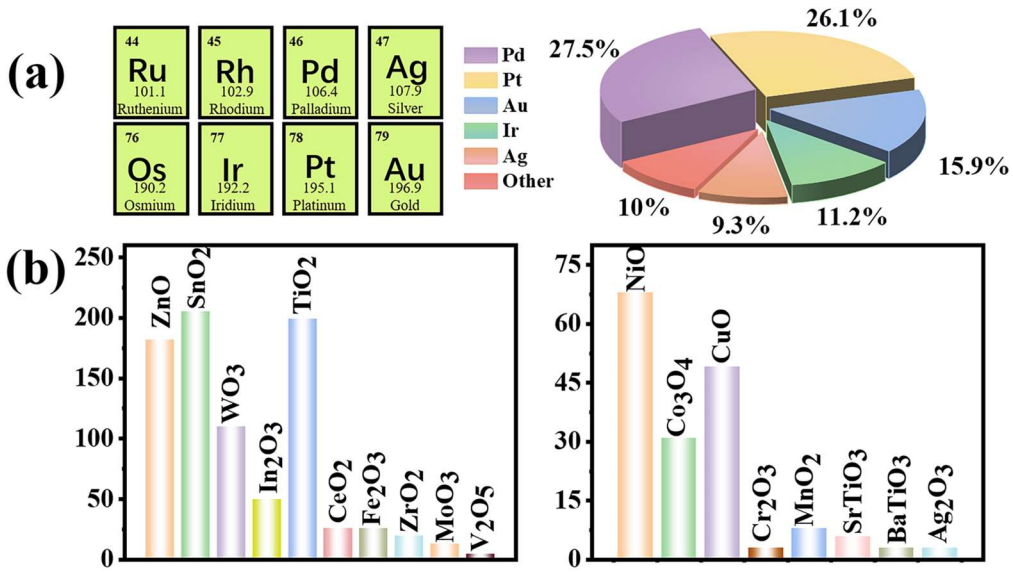

Figure 2. From 2015 to 2024, published articles and patents of noble-metal-decorated MOSs-based H_2 sensors were categorized: (**a**) based on the type of noble metal utilized, and (**b**) based on the specific MOS employed. Data is from the Web of Science.

Despite the successful commercialization of MOS-based H_2 sensors, they operate at relatively high temperatures, ranging from 250 °C to 400 °C, and a significant dependence on humidity. This dependence undermines the reliability of MOS sensors, particularly when operated at room temperature (RT), as noted in [27]. Humidity can interfere with gas–solid interactions by forming water layers, reducing the effective surface area for H_2 adsorption. High temperatures boost energy consumption and accelerate sensor aging, shortening lifespan. Noble metal decorations can mitigate these issues by inhibiting water adsorption and favoring the adsorption and H_2 reactions with a low activation energy, enabling low-temperature operation. Moon et al. [28] improved H_2 detection at RT and reduced humidity impact by modifying SnO_2 with Pd NPs. Lupan et al. [29] showed enhanced H_2 detection at RT and a reduced humidity dependence with Au-NP/ZnO NWs, achieving high selectivity and response. To meet the H_2 sensing performance benchmarks, which include a response time of less than 1 s at a 4% hydrogen concentration and less than 60 s at a 1% H_2 concentration, along with a recovery time of less than 60 s, it is imperative to develop H_2 sensors characterized by faster response and recovery performance [30].

2. Sensing Mechanism

2.1. General Sensing Mechanism of MOSs-Based H_2 Sensors

The general mechanism of chemical impedance MOSs gas sensing can be elucidated as follows [31]: Firstly, the adsorption of oxygen molecules from the ambient air on the metal oxide surface leads to the trapping of electrons and the conversion of oxygen anions as shown in Equations (1)–(4) [32]. Temperature plays a crucial role in the O_2 adsorption and dissociation process. As the temperature increases, the O_2 molecules gain enough energy to undergo chemisorption and capture electrons to form oxygen anions (e.g., O_2^-, O^-, and O^{2-}) [33]. At this point, the sensitivity of the sensor increases significantly, but too high a temperature may lead to too fast a reaction between the target gas and the oxygen anions, reducing the selectivity of the sensor [34]. The adsorption and dissociation temperatures of O_2 vary depending on the sensing material. For example, the reactions of Equations (2)–(4) occur at a temperature below 180 °C, 180 °C~400 °C, and above 400 °C on Pd, respectively. At high temperatures, adsorbed oxygen anions may desorb from the surface, leading to a decrease in the active sites on the sensor surface, thus affecting the sensitivity. Excessive temperatures may also lead to sintering or phase transformation of the MOSs, further degrading the performance of the sensor [27].

$$O_2(gas) \rightarrow O_2(ads), \quad (1)$$

$$O_2(ads) + e^- \rightarrow O_2^-(ads), \quad (2)$$

$$O_2^-(ads) + e^- \rightarrow 2O^-(ads), \quad (3)$$

$$O^-(ads) + e^- \rightarrow O^{2-}(ads), \quad (4)$$

$$H_2(gas) \rightarrow H_2(ads), \quad (5)$$

$$H_2(ads) \rightarrow 2H(ads), \quad (6)$$

$$H(ads) + O^-(ads) \rightarrow OH^-(ads), \quad (7)$$

$$OH^-(ads) + H(ads) \rightarrow H_2O(gas) + e^-, \quad (8)$$

$$4H(ads) + O_2^-(ads) \rightarrow 2H_2O(gas) + e^- \quad (9)$$

In the context of n-type MOSs, such as ZnO and SnO_2, the presence of an electron depletion layer (EDL) on their surface leads to an increase in surface resistance. Conversely, for p-type MOSs, a hole accumulation layer (HAL) forms on the surface of the sensing material, resulting in a decrease in surface resistance.

When exposed to H_2, H_2 molecules adsorb onto the surface of sensing materials, which then reacts with adsorbed oxygen anions present on the MOS surface, as illustrated in Equations (5)–(9). In a H_2-rich environment, the H_2 reacts with adsorbed oxygen anions on the surface to produce water, simultaneously releasing electrons back to the material's surface. For n-type MOSs, this leads to an increase in electron concentration on the outer surface, causing a narrowing of the EDL and resulting in a sensing signal characterized by a reduced resistance value. Conversely, in p-type semiconductors, the emitted electrons decrease the hole concentration, thereby generating a sensing signal marked by an increased resistance value. Furthermore, the specific temperature at which the reactions in Equations (5)–(9) occur is dependent on the sensing material. However, the gas response of conventional MOSs is limited. Therefore, an effective strategy involves the utilization of noble metal nanoparticles for modification.

2.2. Sensing Mechanism of Noble-Metal-Decorated MOSs-Based H_2 Sensors

The modification of MOSs with noble metal nanoparticles, such as Pd, Pt, and Au, represents an efficacious method for enhancing gas response. In comparison to unmodified MOSs, the H_2 sensing behavior and mechanism of noble-metal-loaded MOSs exhibit a significantly higher degree of complexity. This complexity arises from the intricate interplay between the noble metals and the MOSs, encompassing both surface chemistry and electronic coupling [35].

Initially, we focused on the surface chemistry underlying the H_2 sensing mechanism of noble-metal-decorated MOSs. Extensive research has shown that noble metals serve as catalysts, enhancing the adsorption of oxygen onto material surfaces and facilitating the dissociation of target gas molecules. The Schottky barrier, formed at the junction of noble metal electrodes (Pt, Pd, Au, etc.) and the semiconductor material, is recognized as a critical factor in sensing processes. In the context of H_2 sensors based on noble-metal-decorated MOSs, beyond the reactions outlined in Equations (1)–(5), there may also be a phenomenon where oxygen and hydrogen atoms diffuse from the noble metal onto the oxide support. This phenomenon is termed "spillover". Recently, several advanced methodologies have been formulated to gain a deeper understanding of the gas sensing mechanism of noble-metal-decorated MOSs. These methodologies encompass density functional theory calculations and in situ transmission electron microscopy analysis [36,37]. A diverse range of noble-metal-decorated MOSs, including Pd/SnO_2 and Pt/ZnO, have been employed in H_2 sensors. Subsequently, we will discuss the sensing mechanism of a typical Pd/SnO_2 H_2 sensing system as an illustrative example (Figure 3).

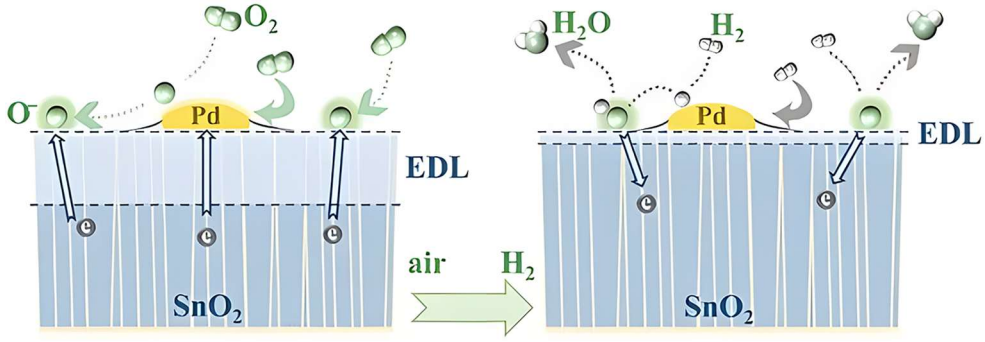

Figure 3. Illustration of the H_2 gas sensing mechanism of Pd/SnO_2 [38].

When pure SnO_2 is exposed to air, O_2 molecules adsorb onto the SnO_2 surface. This adsorption process captures free electrons from the conduction band of SnO_2, forming adsorbed oxygen anions (depending on the operating temperature, as detailed in [39]). Consequently, an EDL forms, leading to an increase in the sensor's resistance.

When Pd at the nanoscale interfaces with SnO_2, it extracts electrons from SnO_2, thereby inducing an EDL at the interfaces [38]. Upon exposure of the Pd/SnO_2 composite to air, the catalytically active Pd facilitates the dissociation of O_2 molecules, with the resultant oxygen atoms subsequently diffusing from the Pd to the SnO_2 support [38] (Figure 3). The diffused oxygen atoms then accept electrons from the bonded SnO_2, leading to the broadening of the EDL.

When the sensor is subjected to H_2, as depicted on the right-hand side of Figure 3, H_2 molecules adsorb onto the Pd surface and disassociate into hydrogen atoms due to the strong affinity of Pd for H_2 [40]. Subsequently, following spillover, the diffused hydrogen atoms primarily interact with adsorbed oxygen anions [38], forming surface hydroxyl groups [41]. These hydroxyl groups exhibit a reduced electron affinity, causing the release of electrons back to SnO_2 upon the desorption of produced H_2O molecules at temperatures

exceeding 100 °C. This process results in a significant narrowing of the EDL and a corresponding decrease in its resistance [42]. Note that, following the spillover, the active sites on Pd for O_2 and H_2 molecule adsorption and dissociation are freed and become available to capture additional O_2 and H_2 molecules, thereby initiating a new reaction cycle.

Moreover, H_2 can reduce PdO to Pd (Equation (10)), leading to the cessation of electronic interactions or even the formation of a low-work-function Pd hydrid (PdH_x), which promotes the reverse transfer of electrons [43]. Consequently, the return of a significant number of electrons results in a narrowing of the EDL and a decrease in the sensor's resistance [44]. The initial reduction reaction of PdO_x leads to an increase in the concentration of Pd^0. This process is considered partial and reversible, as reported in [45]. The resultant reduced Pd can subsequently catalyze the reaction between H_2 molecules and adsorbed oxygen anions, as outlined in Equations (5)–(9). This catalysis facilitates the release of electrons into the conduction band of SnO_2, thereby enhancing the conductivity of the composites [46].

$$PdOx + 1/2H_{2(g)} \rightarrow Pd^0 + xH_2O_{(g)} \quad (10)$$

The aforementioned mechanism elucidates the superior sensing performance of noble-metal-decorated MOSs at both room and high temperatures. Notably, Pd has been documented as an exceptionally efficient catalyst for H_2 dissociation, even at low temperatures [32]. Meng et al. [47] proposed that, in addition to the adsorption of H_2 and O_2 on Pd surfaces, electron sensitization of Pd can also facilitate the redistribution of interfacial electrons (Figure 4a). Considering the example of 1.0 at% $Pd/SnS_2/SnO_2$, the metal-semiconductor interface exhibits distinct phenomena due to the difference in work functions. Specifically, the work function of Pd is higher than that of the SnS_2/SnO_2 semiconductor (Figure 4b). Consequently, the energy band in the semiconductor shifts downward, resulting in the formation of Schottky barriers at the metal–semiconductor interface. Within the 1.0 at% $Pd/SnS_2/SnO_2$ composition, Pd exists not only in its metallic form, but also as PdO. Notably, the work function of PdO (ϕ = 7.9 eV) is higher than that of SnS_2/SnO_2, prompting electrons to transfer from SnS_2/SnO_2 to PdO, leading to the formation of a p–n heterojunction (Figure 4c). The concurrent generation of Schottky barriers and p–n heterojunctions broadens the EDL in SnS_2/SnO_2, thereby increasing the baseline resistance ($R_a \approx 225\ M\Omega$). Upon exposure of $Pd/SnS_2/SnO_2$ to H_2, a portion of Pd converts to PdH_x, characterized by a lower work function ($\varphi < 4.4$ eV, Figure 4d). This shift causes electrons to flow from PdH_x back to SnS_2/SnO_2, increasing the electron concentration in SnS_2/SnO_2 and subsequently decreasing the resistance (R_g) of the $Pd/SnS_2/SnO_2$ material. These synergistic effects result in a significant variation in resistance and contribute to the excellent sensing characteristics of the material.

The small amount of Pd could exhibit three distinct functionalities: catalyzing the dissociation of O_2 molecules, catalyzing the dissociation of H_2 molecules, and exerting a direct influence on the thickness of the EDL. Among these functionalities, the primary role of Pd is likely to serve as a catalyst for H_2 dissociation, attributed to its efficient capability to facilitate this process even at a low temperature—a pivotal advantage in the context of H_2 sensing applications. Nevertheless, the significance of the other two roles should not be overlooked. When Pd is deposited onto MOSs, it can further influence the sensor's response characteristics via complex interactions between Pd and the MOSs. These interactions encompass various facets, including interface chemistry and electronic coupling mechanisms, which collectively govern the overall performance of the sensor.

In summary, due to the interaction between noble metals and MOSs, the H_2 sensing mechanism of noble-metal-loaded MOSs is complex, and many aspects such as surface chemistry and electronic coupling need to be considered.

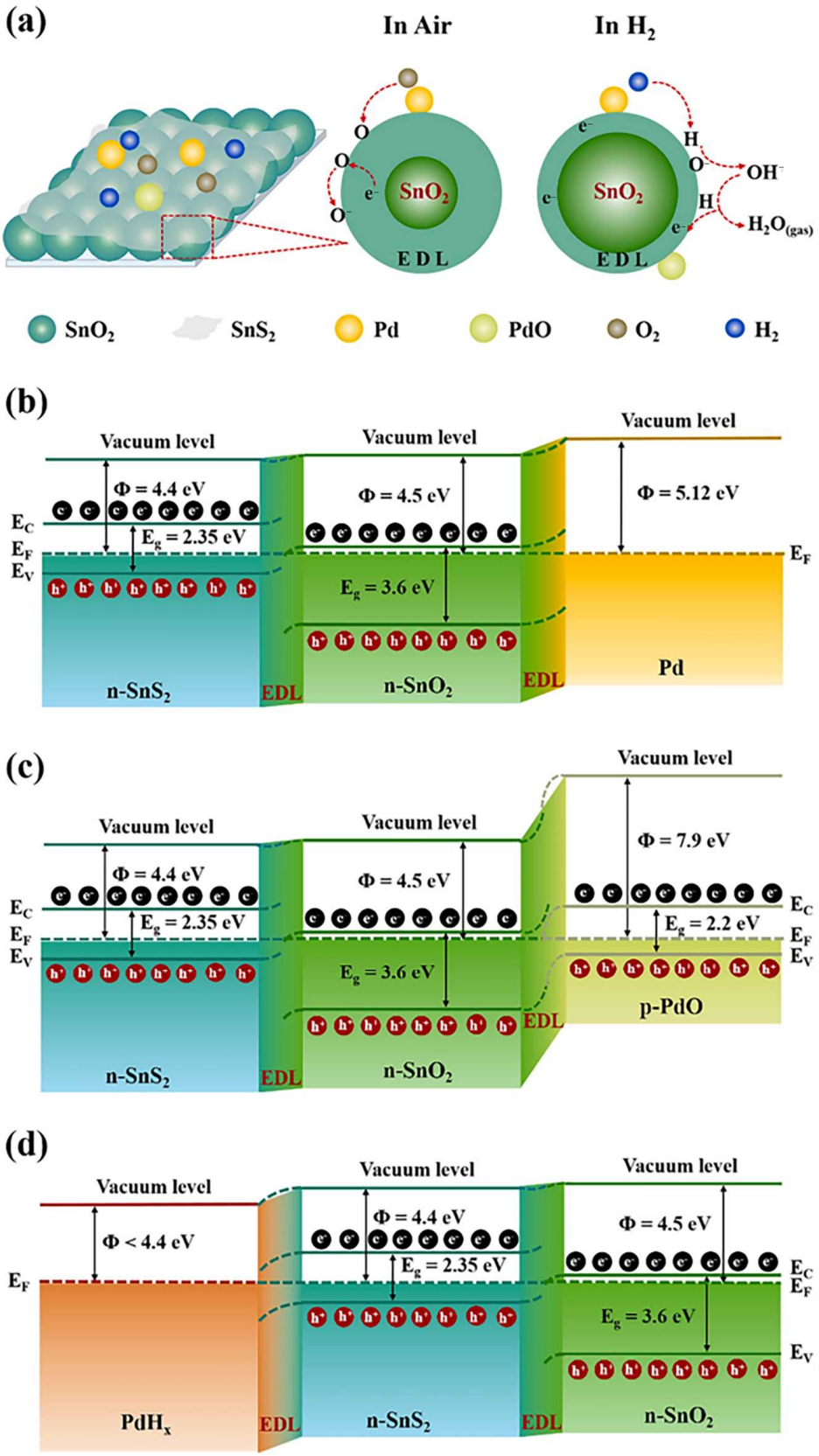

Figure 4. (**a**) Schematic diagram of the $Pd/SnS_2/SnO_2$ H_2 sensing mechanism. The band structure of (**b**) $Pd/SnS_2/SnO_2$, (**c**) $PdO/SnS_2/SnO_2$ and (**d**) $PdH_x/SnS_2/SnO_2$ [47]. Reprinted with permission from Elsevier, copyright 2022.

3. Noble-Metal-Decorated MOSs-Based Gas Sensors

3.1. Pd-Decorated MOSs-Based Gas Sensors

Pd-decorated MOSs exhibit heightened sensitivity, remarkable selectivity, fast response/recovery times, and low detection limits for H_2 sensing, attributable to the distinct solubility of H_2 in Pd and its capacity to form PdHx. Notably, only H_2 is capable of inducing significant lattice expansion in Pd, due possibly to the small radius of the hydrogen atom, whereas other gases such as carbon monoxide (CO) exhibit no such effect. This specificity contributes to the excellent selectivity of the Pd-based sensor. The processes of hydrogen adsorption and desorption on Pd occur rapidly, facilitating fast response and recovery. Furthermore, the rapid diffusion and high solubility of hydrogen atoms within the Pd lattice result in substantial resistance changes even at trace concentrations of H_2, enabling low detection limits.

Given these advantages, Pd catalysts are extensively utilized for H_2 detection. Various studies have shown that the reduction of Pd precursors can be accomplished through solution-based methods involving UV light irradiation [48], chemical reducing agents [49], and thermal treatments [50].

3.1.1. Pd-Decorated SnO_2

Among the diverse array of semiconductors, n-type SnO_2, characterized by its wide band gap of 3.5~4.0 eV [51,52], which can be measured via photocurrent spectroscopy [53], stands out as a promising candidate for sensing applications due to its low cost, simple manufacturing technique, and good long-term stability. However, its application is hindered by limitations such as low sensitivity, high operational temperature, inadequate selectivity, and sluggish response kinetics. To overcome these disadvantages, the modification of SnO_2 through the incorporation of other materials, particularly noble metals such as Pd, has proven to be an effective strategy for improving its sensing performance.

Manipulating the dimensionality [54–57] and dispersion of Pd on MOSs supports can fine-tune their H_2 sensing performances. So far, a number of Pd-based H_2 sensors, including nanowires (NWs) [5,58,59], nanosheets (NSs) [60], nanofibers (NFs) [59,61], nanoflowers [62], nanorods (NRs) [63,64], nanotubes (NTs) [65,66], and films have been suggested [47].

The nanoparticles (NP) enhance sensor sensitivity by providing a larger surface area for gas adsorption. Nam et al. [67] (Table 1) fabricated Pd/SnO_2 nanoparticles (NPs) for an exceptionally sensitive and selective H_2 gas sensor by leveraging Pluronic F-127 (Figure 5). Pluronic F-127, a block copolymer structured as (polyethylene oxide)99-(polypropylene oxide)69-(polyethylene oxide)99 [68], features three hydrophilic chains and a central hydrophobic chain. It functions dualistically as a reducing agent and surfactant, enhancing the dispersion of Pd NPs and modulating their size. In comparison to pristine SnO_2 and Pd/SnO_2 NPs synthesized without the aid of F-127, the Pd/SnO_2 NPs synthesized with F-127 assistance, denoted as F-Pd/SnO_2, exhibited a superior H_2 response of 27, 190 and a fast response time of 3 s when exposed to 50 ppm of H_2 at 100 °C (Figure 5). This enhancement is attributed to the increased number of nanojunctions.

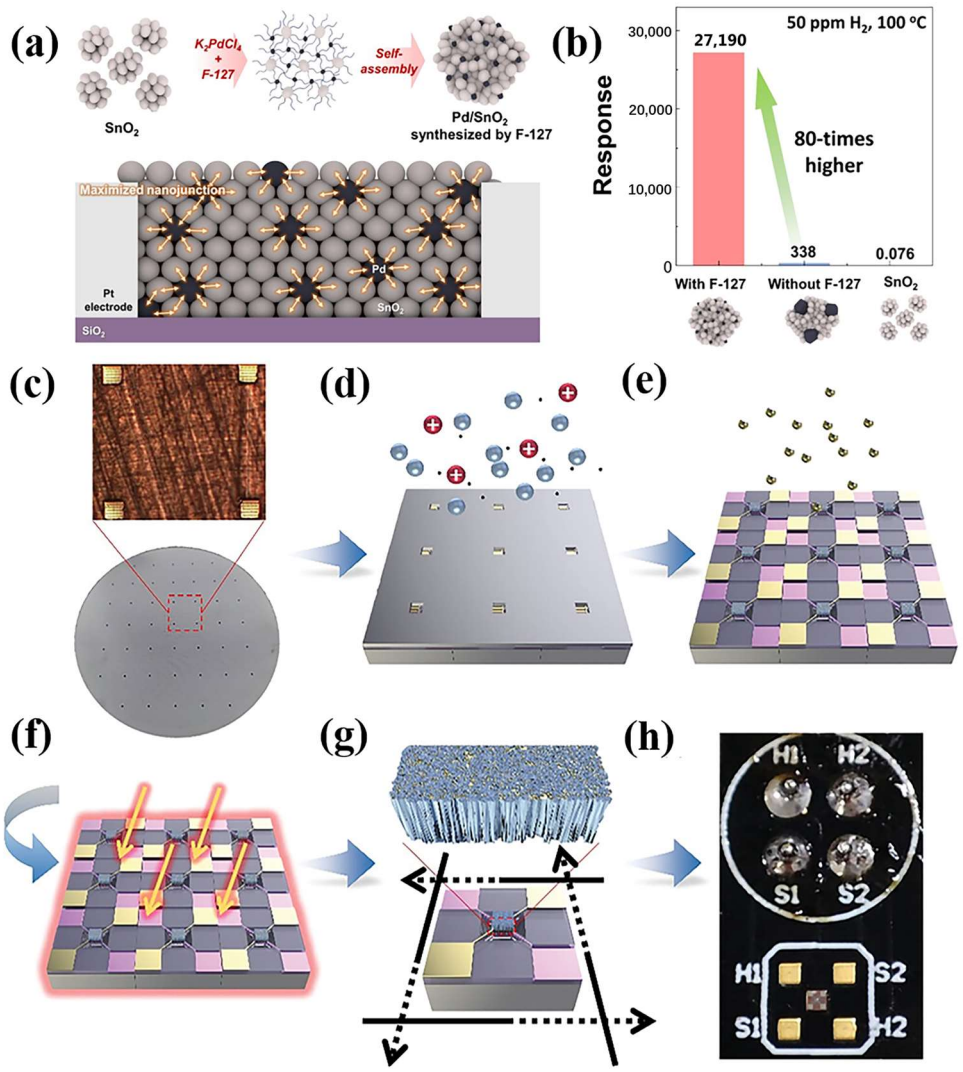

Figure 5. (**a**) Schematic illustration of the synthesis mechanism of F-Pd/SnO_2 nanoparticles with Pluronic F-127 assistance and corresponding response comparison plot of SnO_2, Pd/SnO_2 [69]. Reprinted with the permission from Elsevier, copyright 2024. (**b**) F-Pd/SnO_2 to 50 ppm of H_2 at 100 °C [69]. (**c**) Schematic of the fabrication of Pd/SnO_2 sensing film patterns and MEMS H_2 sensing chips: The micro hotplate arrays are aligned with the mask [38], (**d**) SnO_2 film patterns are deposited in the central sensing area by a mask-assistant magnetron sputtering method [38], (**e**) Pd NPs catalysts are further decorated on SnO_2 by ALD [38], (**f**) the film patterns perform annealing treatment in air-H_2-air, and finally the MEMS H_2 sensing chips are obtained after (**g**) dicing and (**h**) wire bonding [38].

In the above work and some other literature [47], H_2 sensors utilizing SnO_2 nanostructures exhibit linear response characteristics within a concentration range of up to 1% H_2. Only a few works reported H_2 sensing properties at concentrations exceeding this threshold. For H_2 concentrations ranging from 1% to 2%, detection utilized the volumetric expansion characteristic of the β-phase PdH_x. This expansion arises from the phase transition from α-Pd to β-PdH_x, causing the reconnection of previously disrupted junctions within the Pd, thereby resulting in a fast decrement of the resistance in Pd-based sensors [69].

Table 1. The comparison of sensing performances of noble-metal-decorated MOSs.

Materials	Optimal Temperature (°C)	τ_{res}/τ_{rec} (s)	Detection Limit (ppm)	Concentration (ppm)	Response	Ref.
F-Pd/SnO_2	100	3/NA [a]	50	50	27,190 [c]	[67]
30Pd/SnO_2	150	NA/30 [a]	0.5	20	1.51 [d]	[38]
Pd/SnS_2/SnO_2	300	1/9 [a]	10	500	90 [d]	[47]
Pd/SnO_2	210	3.4/5.6 [a]	1.5	5000	712.65 [e]	[35]
SnO_2-Pd@rGO	390	8/3 [a]	0.1	200	243.5 [f]	[32]
NiO-shelled Pd-decorated ZnO NW	200	NA	NA	100	13.36 [d]	[62]
Pd@ZnO-2	350	84/468 [a]	NA	100	22 [d]	[70]
Pd/Fe_2O_3-NiO NFs	250	11/105 [a]	1	1000	199.24 [d]	[71]
p-PdO-*n*-WO_3-heterostructure film	160	4/NA	0.5	100	45.1 [d]	[72]
Pt SnO_2–Co_3O_4	300	12/NA	NA	100	57.9 [d]	[73]
Pd-doped rGO/ZnO-SnO_2	380	4/8 [a]	9.4	100	9.4 [d]	[74]
5.0 wt% Pd NPs/CeO_2-C	25	3/NA [a]	NA	100	1322 [d]	[75]
Pt-TiO_2-MoS_2	100	NA	50	500	47.09 [d]	[76]
Pt-SnO_2	25	13/NA [a]	NA	1000	5000 [e]	[77]
Pt-SnO_2	825	NA	NA	1000	450 [e]	[78]
ZnO–Pt	300	133/112 [a]	100	1000	132.5 [g]	[79]
WO_3/Pt-ZnO	R.T.	19/81[a]	1	100	61.5 [d]	[80]
ZNT/G	R.T.	30/38 [a]	10	100	28.08 [d]	[81]
MoS_2-HIZNTs	R.T.	14/19 [a]	10	500	51.1 [h]	[82]
Pt–Fe_2O_3–V_o	240	2/45 [b]	0.086	50	NA	[83]
PtRu/CeO_2	500	97/123 [a]	100	100	NA	[84]
Ag@SnO_2@g-C_3N_4	300	¾ [a]	0.03	50	5.4 [d]	[85]
Ir_{red}/ZnO-450	450	7/9.7 [a]	10	100	5.5 [d]	[86]

[a]: The response time (τ_{res}) and the recovery time (τ_{rec}) were determined as the time taken for the resistance (current) to reach 90% of the saturated response upon exposure to H_2 and to decrease by 90% back to baseline after removal, respectively. [b]: $\tau = \upsilon_0^{-1}\exp\left(\frac{-E_{ads}}{TK_B}\right)$. υ_0, K_B, and T are the attempt frequency, Boltzmann constant, and temperature. [c]: $R = (R_a - R_g)/R_g$. R is the sensor response. R_a and R_g are the sensor resistance in air and target gas, respectively. [d]: $R = R_a/R_g$. [e]: $\triangle I/I_0 = [(I - I_0)/I_0] \times 100\%$. I and I_0 represent the current values under target gas and baseline (no target gas) conditions, respectively. [f]: $R = I_g/I_0$. [g]: $R = (G_g - G_a)/G_a \times 100\%$. G_g and G_a are the conductance of H_2 gas and air stimulation at different ppm of the sensor, respectively. [h]: $R = R_a/R_g \times 100\%$. NA: Not available.

A comprehensive elucidation of the H_2-sensing mechanism at concentrations above 1% is required. Liu et al. (Table 1) have proposed the existence of two H_2 concentration-dependent sensing mechanisms for their developed Pd/SnO_2 NPs film-based H_2 sensor, designed for H_2 detection across a wide concentration range (1.5 ppm to 10%) [35]. Specifically, below a 1% H_2 concentration, the sensor response exhibits a linear correlation with the square root of the H_2 concentration, primarily attributed to the electronic coupling effect occurring at the interface between PdH_x and SnO_2. This mechanism facilitates a high sensitivity of 0.23 ppm^{-1}. As the H_2 concentration increases beyond this point, a linear dependence between the response and H_2 concentration is observed, with a sensitivity of 0.018 ppm^{-1}. This latter behavior is attributed to the redox reaction between H atoms and the adsorbed oxygen anions on the SnO_2 surface [35].

SnO_2-based H_2 sensors show a high compatibility with integrated circuits (IC). The development of intelligent and integrated H_2 sensors has emerged as a focal area of contemporary research. As gas sensing chips transition into mass production, a multitude

of challenges have come to light. Achieving a uniform film at the wafer level is a pivotal prerequisite for ensuring high consistency among sensing chips. However, conventional techniques such as drop-coating and screen-printing fall short at meeting this criterion due to their inherent lack of precision and uncontrollability. Furthermore, these methods often lead to unwanted contact between sensing materials and electrode pads, thereby inducing signal crosstalk between the heating and testing electrodes, and potentially compromising the subsequent packaging process. Consequently, the development of effective gas sensing film patterning methods and noble metal catalytic modification techniques at the wafer level is of paramount importance for the mass manufacturing of sensing chips. Recently, Zhang et al. [38] (Table 1) have devised a straightforward methodology that integrates atomic layer deposition (ALD), magnetron sputtering, and subsequent annealing in an air-H_2-air atmosphere to fabricate high-performance Pd/SnO_2 film patterns tailored for H_2 sensing (Figure 3). This approach allows for precise regulation of the grain size and crystallinity of the Pd/SnO_2 films through meticulous control of the deposition and annealing processes, ultimately enhancing their H_2 sensing capabilities. The resultant MEMS H_2 sensing chips exhibit remarkable consistency and a broad detection range spanning from 0.5 to 500 ppm. Notably, even at an H_2 concentration as low as 0.5 ppm, a discernible change in resistance and response value (with a signal-to-noise ratio exceeding 3) is observed [38]. This sensing chip boasts a lower detection limit and an expanded detection range encompassing three orders of magnitude compared to certain previously reported H_2 sensors [38]. Two problems may be encountered regarding thin films such as film uniformity and signal crosstalk, which can be further explored with more advanced deposition techniques, as well as with new patterning methods. A combination of deposition techniques and patterning methods can be used to significantly improve the performance of H_2 sensors. For example, ALD deposits a uniform film and combines it with an isolation trench design to reduce signal crosstalk or deposit a uniform catalytic layer by sputtering. Adding a shielding layer also blocks electric field interference [87].

In addition to the decoration with noble metals, the further modification of SnO_2 with alternative semiconductors offers a viable approach to enhancing its H_2 sensing capabilities, primarily due to the substantial resistance modulation at heterojunction barriers. Various semiconductors have been utilized to establish heterojunctions with SnO_2 and are co-supported with noble metals [88]. Notably, 2D semiconductors have emerged as prominent candidates owing to their layered structure, high surface-to-volume ratio, unique semiconducting attributes, and substantial electronegativity [89]. Tin disulfide (SnS_2), for instance, exhibits considerable potential in heterostructure-based sensing applications. Meng et al. (Table 1) synthesized SnO_2@SnS_2 hollow nanostructures through a combined hydrothermal and impregnation approach [47]. The optimized 1.0 atomic percent (at%) Pd/SnS_2/SnO_2 nanocomposites exhibited a peak response of 95 towards 500 parts per million (ppm) H_2 at 300 °C (Figure 6a), which was 10.6 times higher than that of pure SnO_2 nanoparticles and 5.3 times higher than that of pure SnS_2/SnO_2-2 nanocomposites [47]. Furthermore, the 1.0 at% Pd/SnS_2/SnO_2 composites demonstrated rapid response and recovery times of 1 and 9 s (Figure 6b), respectively, along with exceptional selectivity and stability [47]. The enhanced H_2 sensing properties of the Pd/SnS_2/SnO_2 nanocomposites may be attributed to several factors: (1) the spillover effect of Pd, (2) the formation of a Schottky barrier at the interface between Pd and SnS_2/SnO_2, and (3) the establishment of a p-n heterojunction at the junction between PdO and SnS_2/SnO_2.

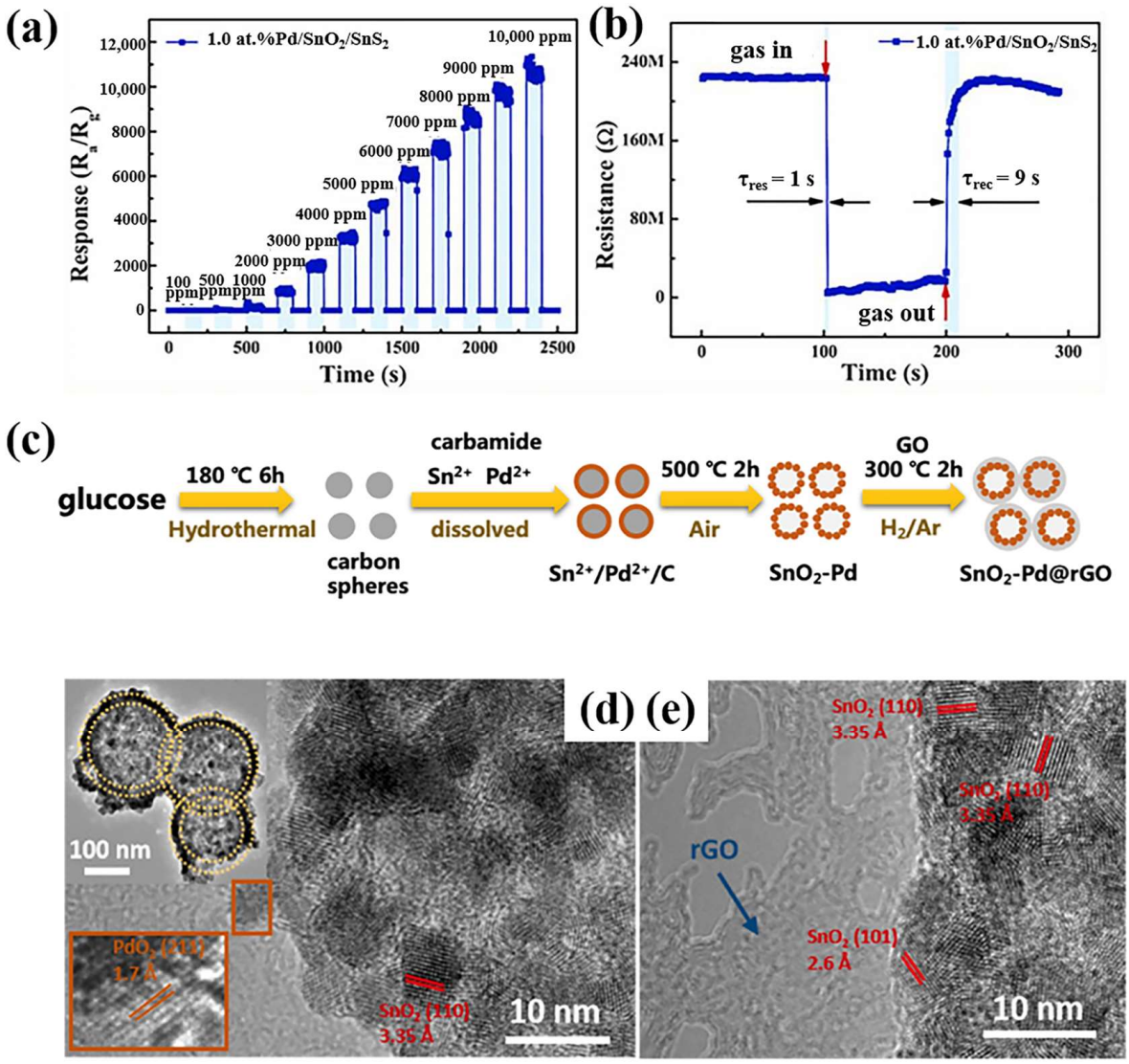

Figure 6. (**a**) Response curves and (**b**) response/recovery time of $Pd/SnS_2/SnO_2$ towards 500 ppm H_2 [47]. Reprinted with permission from Elsevier, copyright 2022. (**c**) The schematic for the rGO-wrapped SnO_2–Pd hollow porous spheres. SnO_2–Pd@rGO: (**d**) TEM image (inset: high-resolution HRTEM image), (**e**) HRTEM image [32]. Reprinted with permission from Elsevier, copyright 2022.

Apart from SnS_2, graphene and reduced graphene oxide (rGO) have been extensively employed to construct heterojunctions with MOSs to achieve impressive gas sensing performances, attributed to their large specific surface areas and exceptional electron mobility [32]. Notably, the hydrophobicity of rGO has been confirmed to suppress the effects of high humidity on graphene-based gas sensing [90]. Qiu et al. (Table 1) fabricated an rGO-encapsulated SnO_2–Pd porous hollow sphere composite (SnO_2–Pd@rGO) for a high-performance H_2 sensor [32]. The porous hollow architecture of this composite was derived from a carbon sphere template (Figure 6c). The encapsulation with rGO was achieved through the self-assembly of GO onto SnO_2-based spheres, followed by thermal reduction in a H_2 atmosphere (Figure 6c). This sensor demonstrated outstanding selective H_2 sensing characteristics at 390 °C, exhibiting a linear response across a broad concentration range (0.1–1000 ppm) with a fast recovery time of 3 s. It also showed a high response of approximately 8 to 0.1 ppm H_2 within one minute and maintained acceptable stability under high humidity conditions (e.g., 80%). The calculated detection

limit of 16.5 ppb facilitated the potential for trace H_2 monitoring. Furthermore, the sensor displayed a detectable response to H_2 at a minimum concentration of 50 ppm at 130 °C. These remarkable performances were primarily attributed to the unique hollow porous structure with abundant heterojunctions (Figure 6d,e), the catalytic activity of doped-PdO_x, the relatively hydrophobic surface provided by rGO, and the deoxygenation process following H_2 reduction.

The chemiresistive gas sensing mechanism of the MOSs composite is attributed to both electronic sensitization (i.e., energy band modulation and heterojunction formation) and chemical sensitization (i.e., doping spillover and oxygen adsorption) [91]. In the context of electronic sensitization, heterojunctions are established between p-type rGO and n-type SnO_2. The disparity in their work functions (5.1 eV for rGO and 4.5 eV for SnO_2) [92] leads to the formation of an electron depletion region on the SnO_2 side at the SnO_2/rGO interface.

Notably, the experimental evidence revealed that the SnO_2–Pd@rGO composite predominantly comprises PdO and PdO_2 phases, accounting for 96.1% of the total Pd content. The doped PdO_x species are recognized as potent electron acceptors exhibiting p-type behavior, which can effectively lower the Fermi level of SnO_2. Consequently, an additional electron depletion region is induced on the SnO_2 side at the SnO_2/Pd interface. Furthermore, PdO_2, being metastable and more reactive towards the target gas compared to PdO [93], is likely advantageous for enhancing the H_2 sensing performance of the SnO_2–Pd@rGO composite, given the substantial presence of PdO_2 in the material.

3.1.2. Pd-Decorated ZnO

As discussed above, SnO_2 exhibits high conductivity and remarkable sensitivity to low gas concentrations, particularly enabling a swift response to variations in H_2 concentration and generating pronounced electrical signal changes in H_2 sensors. However, ZnO offers several advantages over SnO_2 in the context of H_2 sensors utilizing MOSs. Specifically, ZnO boasts superior biological adaptability, safety, unique piezoelectric properties, and potential fabrication process and cost benefits. Consequently, in certain specific applications, ZnO may be a more suitable sensing material for H_2 sensors.

Nonetheless, the sensing application of pure ZnO is constrained by its low response, instability, and particularly poor H_2 selectivity. To address these limitations, functionalizing ZnO with noble metal catalysts, such as Pd and Pt, presents a promising approach to enhance the properties of the material [70].

The presence of relatively high humidity leads to a decreased gas response in ZnO sensors, owing to competition for adsorption sites on the sensor surface between H_2O molecules and H_2 molecules [94]. Nevertheless, the incorporation of noble metal NPs has been found to enhance the stability of gas sensors under humid conditions [95].

To enhance the sensing performance by generating abundant active sites, effective approaches involve forming MOSs heterojunctions and modifying the morphology to achieve a larger specific surface area. Controlling the morphology of Pd–ZnO structures can regulate their H_2 sensing capabilities. For instance, Nguyen et al. (Table 1) observed the microscopic morphology of Pd@ZnO-2 using TEM (Figure 7a) [70]. The Pd-decorated ZnO showed improved H_2 sensing performances compared with the ZnO NPs.

However, the operation of gas sensors at high temperatures can lead to the oxidation of ultrafine noble metal particles in the air, thereby reducing sensing performance and causing agglomeration of noble metals on the sensor surface [96]. Therefore, it is crucial to devise a method to shield noble metals from direct air exposure to enhance sensing performance. One effective preservation strategy involves depositing a thin layer of metal oxide on a surface adorned with nano-noble metal particles. Among the candidates for protective layer materials, p-type NiO has garnered significant attention due to its robust structural

stability, exceptional oxygen adsorption capacity, and potent catalytic activity [97]. Badie et al. (Table 1) [60] employed NiO as a deposition layer to coat Zn NWs decorated with Pd (Figure 7b). In the absence of Pd decoration on ZnO, NiO comes into direct contact with ZnO. The intimate contact between n-type ZnO and p-type NiO generates numerous heterojunctions with potential barriers that impede charge flow in air. Upon exposure to the target gas, the barrier height alters, leading to a change in sensor resistance. Since NiO is deposited as a continuous layer, a core-shell structure forms, with ZnO and NiO in direct contact, maximizing the contact area between the components and resulting in substantial resistance variations. Alternatively, when Pd nanoparticles are positioned between ZnO and NiO layers, Zn-Pd-Ni oxide heterojunctions are established [60]. Compared to single-component materials, Zn-Ni oxide heterojunctions exhibit superior performance in gas sensing applications [98].

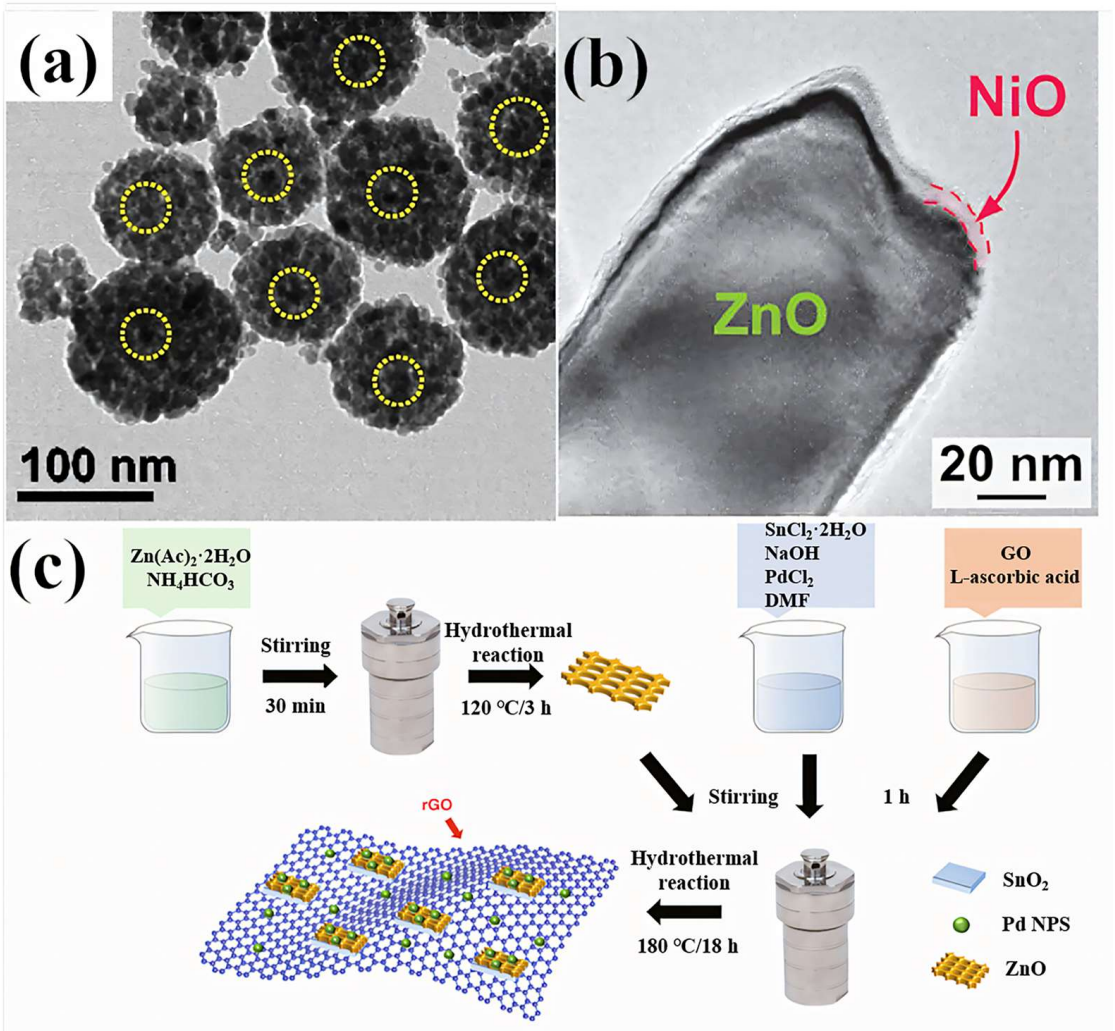

Figure 7. (**a**) TEM observation for Pd@ZnO-2 [70]. Reprinted with the permission from Elsevier, copyright 2020. (**b**) Transmission electron microscope (TEM) image of a NiO-shelled Pd-decorated ZnO NW [60]. Open access. (**c**) The fabrication process of the Pd-doped rGO/ZnO-SnO_2 nanocomposites [74]. Open access.

P-type MOSs, exemplified by NiO as previously mentioned, offer distinct advantages over n-type MOSs in the selectivity and monitoring of reducing gases. This superiority is attributed to the extensive adsorption of oxygen on their surfaces [71]. Research has demonstrated that sensors based on noble-metal-decorated NiO exhibit promising sensing capabilities for H_2 detection [99]. Cai et al. (Table 1) [71] fabricated porous NiO NFs

embedded with Pd and Fe_2O_3 NPs through a straightforward electrospinning process. These sensors achieved a maximum response value of 199.24 for 1000 ppm H_2 gas at an optimal operating temperature of 250 °C, accompanied by a response/recovery time of 11/105 s. Additionally, they exhibited robust selectivity and long-term stability towards H_2. The exceptional gas sensing performance of these sensors is primarily attributed to the catalytic effect of Pd and the unique fluffy porous 1D microstructure, which features tightly linked p-n heterojunctions between NiO and Fe_2O_3. This structure provides a large specific surface area and numerous active sites, thereby facilitating the reaction between H_2 molecules and surface oxygen anions.

Similarly, Zhu et al. (Table 1) [72] observed that Pd in Pd-decorated WO_3 composites exists in the form of PdO, forming a p-n heterojunction. The H_2 gas sensor assembled using the p-PdO-n-WO_3 heterostructure and a uniformly dispersed thin film exhibited excellent sensing performance, high sensitivity, a low detection limit, and good stability. At an optimal operating temperature of 160 °C, the sensor demonstrated response values (R_a/R_g) of 1.2 and 45.1 for H_2 concentrations of 500 ppb and 100 ppm, respectively. Furthermore, the response times were 38 s and 4 s for these concentrations.

In addition to the construction of p-n heterojunctions, the H_2 sensing performance of materials can also be improved by constructing n-n heterojunctions and/or adding other components. For example, Zhang et al. (Table 1) [74] prepared quaternary nanocomposites (Figure 7c) by hydrothermal method using Pd-doped rGO/ZnO-SnO_2 for use as sensing materials in H_2 sensors. Compared with ZnO-SnO_2 composites, the materials doped with 3 wt% rGO (NC3) exhibited a better H_2 response. The maximum H_2 response of the NC3 material at 380 °C is 9.4, which is two times that of NC0, i.e., ZnO-SnO_2.

Oxygen vacancies, a prevalent and crucial type of crystal defect, play a significant role in the sensing performance of these semiconductors [100]. Various strategies have been proposed to enhance the oxygen vacancy content. Traditional methods, such as high-temperature gas reduction and calcination, are commonly employed to create oxygen defects [56,101–106]. However, these methods often require complex or hazardous conditions, including high temperatures and H_2-rich atmospheres. Consequently, the use of an appropriate reducing agent to regulate the concentration of oxygen vacancies at RT has become increasingly important. Ascorbic acid, for instance, serves as an effective reducing agent, promoting the formation of both surface and intrinsic hydroxyl groups. The hydroxyl-oxygen vacancy model introduces a novel mechanism for the generation of oxygen vacancies, wherein hydroxyl groups and oxygen vacancies coexist, with the latter providing accommodation space for adjacent hydroxyl groups. Song et al. (Table 1) [75] developed a "hydroxyl-oxygen vacancy model" utilizing the redox-capable $Ce^{4+} \leftrightarrow Ce^{3+}$ system (Figure 8). Following ascorbic acid reduction, Pd NPs-modified cerium dioxide (CeO_2) (in cubic, Figure 8b, rod-shaped, and spherical morphologies) exhibits a high abundance of hydroxyl groups [75]. This approach not only facilitates the formation of oxygen vacancies within the CeO_2 lattice, but also establishes a linear correlation between the surface Ce^{3+} content, the content of oxygen vacancies, and highly reactive oxygen species [75]. The optimal 5.0 wt% Pd NPs/CeO_2-C, characterized by the highest concentration of oxygen vacancies and Ce^{3+} content, owned the largest EDLs in air (Figure 8a). It demonstrated rapid sensing kinetics (3 s for 1% H_2 and 2 s for 3% H_2, Figure 8c,d) and remarkable sensitivity to H_2 (R_a/R_g of 1322 for 1% H_2), with a detection limit as low as 50 ppm [75].

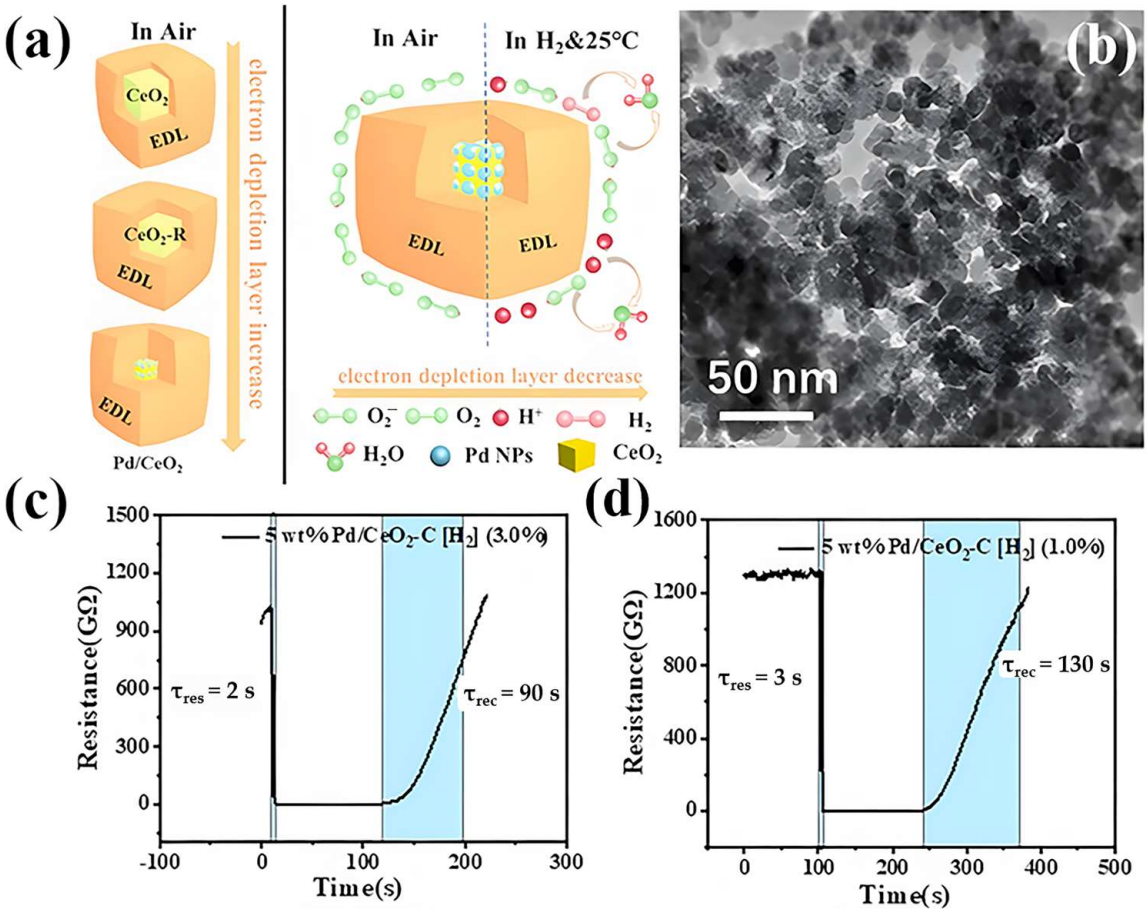

Figure 8. (**a**) Mechanistic diagram of the 5 wt% Pd NPs/CeO_2-C sensor [75]. (**b**) TEM images of 5 wt% Pd NPs/CeO_2-C5 wt% Pd NPs /CeO_2-C [75]. (**c**) Variation of response times of different proportions of 5 wt% Pd NPs CeO_2 at 25 °C in 10,000 ppm H_2 in 1% and (**d**) 3% H_2 concentration [75]. Reprinted with permission from Elsevier, copyright 2023.

3.2. Pt-Decorated MOSs

Pt is also widely used for the H_2 detection. Compared with Pd, Pt has a lower affinity for H_2 molecules, is less prone to H_2 embrittlement, and has better long-term stability. And under certain extreme conditions (e.g., high temperature, strong acid and alkali environment), Pt may exhibit higher stability. Due to the high catalytic activity of Pt, Pt can quickly promote the reaction of H_2 with the sensor surface. Therefore, when Pt is used as a catalyst, the response speed of the H_2 sensor is usually faster, and when the H_2 concentration decreases, the sensor doped with Pt is usually able to return to its initial state more quickly. Accordingly, Pt-decorated MOSs-based H_2 sensors show great potential in applications that require high sensitivity, high selectivity, and a fast response.

3.2.1. Pt-Decorated SnO_2

In practical applications within the realm of gas sensors, SnO_2-based gas sensors continue to be a leading choice. Various strategies have been employed to enhance the gas sensitivity of Pt-decorated SnO_2-baed H_2 sensors, including the construction of n-n, p-n, and p-p heterojunction composites [107–109], the design of hierarchical structures, and the addition of catalytic layers. Luo et al. (Table 1) [76] successfully synthesized a ternary Pt–TiO_2/MoS_2 composite through a two-step hydrothermal method, combining TiO_2 nanoparticles with flower-like MoS_2 structures and depositing Pt. The optimal composites exhibited remarkable sensitivity and selectivity towards H_2 at 100 °C. Similarly, Yin et al. (Table 1) [73] prepared SnO_2–Co_3O_4 p-n heterojunction-based Pt sensing materials via a

hydrothermal method, which demonstrated excellent gas sensitivity and selectivity for H_2 at an optimal operating temperature of 300 °C with an optimal amount of 5% Co.

The long-term stability of MOSs-based sensing materials at RT is crucial for H_2 sensors, as it represents a significant hurdle to their commercialization. Huang et al. (Table 1) [77] addressed this challenge by preparing 1 wt% Pt-doped Pt–SnO_2 nanocomposites that exhibit impressive room-temperature H_2 sensing capabilities. However, these capabilities diminished rapidly over time. Specifically, after seven days of aging, the response to 1% H_2 at RT decreased by a factor of 50. Notably, gentle heat treatment (e.g., 10 min at 140 °C) fully restored the room-temperature H_2 sensing performances of the aged sample. In contrast, the robust response of the Pt–SnO_2 nanocomposite with 5 wt% Pt to 1% H_2 at RT, synthesized by Zhu et al. (Table 1) [78], remained nearly unchanged after six months of aging. However, the recovery rate in air decreased significantly.

3.2.2. Pt-Decorated ZnO

Analogous to Pt-decorated ZnO, the ZnO morphology impacts the sensing properties of Pt-decorated ZnO-based H_2 sensors.

In the work conducted by Uddin et al. (Table 1) [79], the ZnO morphology was optimized through rapid thermal annealing, resulting in an optimal pencil-like topography sensing material suitable for industrial applications up to 300 °C. Additionally, Tan et al. [80] directionally grew ZnO NR arrays on glass substrates and subsequently coated them with WO_3/Pt (Figure 9a,b). Benefiting from the advantages of effective carrier transport in nanoarrays, the high catalytic efficiency of Pt clusters, and the work function of WO_3 NPs, the optimal materials exhibited exceptional H_2 sensing performances, achieving a response of 61.5 to 100 ppm H_2 with response and recovery times of 19 and 81 s, respectively.

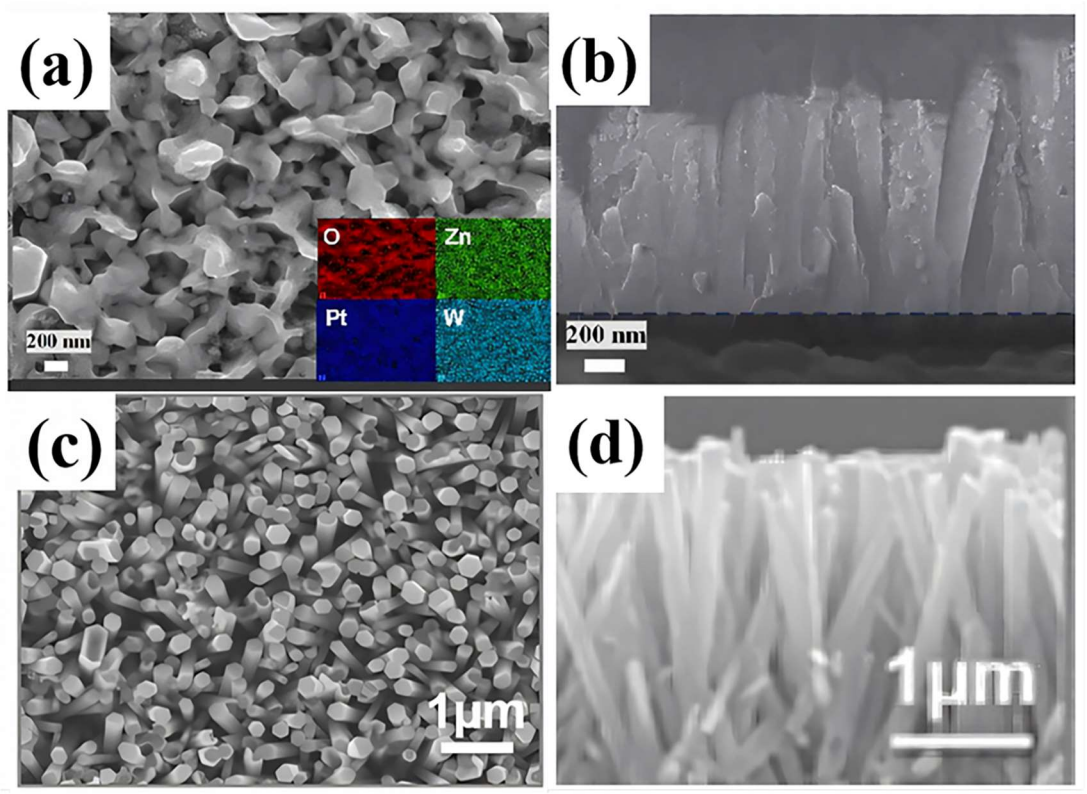

Figure 9. (**a**,**b**) SEM image and cross-sectional SEM of $WPt_{0.25}$/ZnO and the elemental distribution. [80] Reprinted with permission from Elsevier, copyright 2024. (**c**) Field emission SEM images of the optimal ZNT/G. (**d**) The TEM microstructure cross sections of the optimal ZNT/G [81]. Reprinted with permission from [81]. Copyright {2017} American Chemical Society.

Furthermore, ZnO NTs (ZNTs) are also employed in gas sensing applications due to their advantages of having a larger surface area, higher surface oxygen vacancy concentration, and an elevated surface-to-volume ratio [81]. However, ZNTs suffer from limitations such as poor selectivity, stability, and operating temperatures, which impede their progress in gas sensing. These challenges can be addressed by the preparation of hybrid nanocomposites [110]. Kathiravan et al. (Table 1) [81] documented the innovative nanostructural interfaces of self-assembled hierarchical ZnO NTs/graphene (ZNT/G) composites by systematically modulating the growth times of ZNTs on graphene substrates (Figure 9c,d). The optimal ZNT/G sensor demonstrated exceptional repeatability, reliability, and sustained long-term stability over a period of 90 days during hydrogenation/dehydrogenation cycles [81]. This superior performance was attributed to the formation of a robust metallized region at the ZNT/G interface, facilitated by the inner and outer surfaces of the ZNTs, which collectively established a multifaceted depletion layer. Vivekanandan et al. (Table 1) [82] constructed a hybrid structure comprising MoS_2-incorporated ZnO hollow NTs (MoS_2-HIZNTs). This hybrid nanostructure was synthesized through a simple soft-chemical method involving the etching of ZNTs in an aqueous solution with MoS_2 serving as an inducible candidate. The resulting MoS_2-HIZNT material exhibits a unique labyrinth-like structure, leading to exceptional H_2 sensing performance at RT. The enhanced surface area of MoS_2-HIZNTs facilitates the adsorption of more gas ions, resulting in a linear increase in oxygen vacancies and surface-active sites.

As discussed in Section 3.1.2, the oxygen defects in MOSs nanomaterials possess a unique electronic structure and unsaturated coordination environment, which facilitates molecular adsorption and electron transfer in sensing reactions [111]. In addition to ZnO, both iron(III) oxide (Fe_2O_3) [112] and CeO_2 can enhance their H_2 sensing performances through the introduction of oxygen defects. Zhang et al. (Table 1) [83] reported a stable H_2 sensor based on Pt single atoms (Pt SA) anchored to oxygen-rich vacancies on Fe_2O_3 NSs (Pt–Fe_2O_3–Vo) (Figure 10). The surface oxygen vacancies were introduced in the last step under the reducing condition (Figure 10a). Gas sensing studies revealed that at an optimal temperature of 240 °C, the sensor response of Pt–Fe_2O_3–Vo was improved by a factor of 17 compared to pure Fe_2O_3 (Figure 10f), with an ultra-fast response time of 2 s (Figure 10g). It also delivered excellent selectivity, as illustrated in Figure 10h. The exceptional sensing performance of Pt–Fe_2O_3–Vo is attributed to the unique morphology (Figure 10b–e), which favored oxygen spillover. Experimental and density functional theory (DFT) calculations [113] demonstrated that the Pt-Fe atomic site at the oxygen vacancy exhibits higher binding energy, leading to a strong electronic interaction between Pt and the Fe_2O_3 surface, which stabilizes the Pt SA and enhances the sensing performance. CeO_2, characterized by numerous intrinsic defects, possesses various intriguing properties such as oxygen-rich defects, significant redox properties, high oxygen storage capacity, and the ability to absorb and release oxygen through the conversion between Ce_3^+ and Ce_4^+. These attributes of CeO_2 are highly promising for exceptional gas sensing performance. Kim et al. (Table 1) [84] developed CeO_2 hollow NFs (Figure 10i,j) through electrospinning to enhance the interaction between oxygen vacancies (Figure 10k) and H_2 on PtRu, resulting in higher selectivity and a broader detection range (100 ppm to 50%) compared to the CeO_2 and Pt/CeO_2.

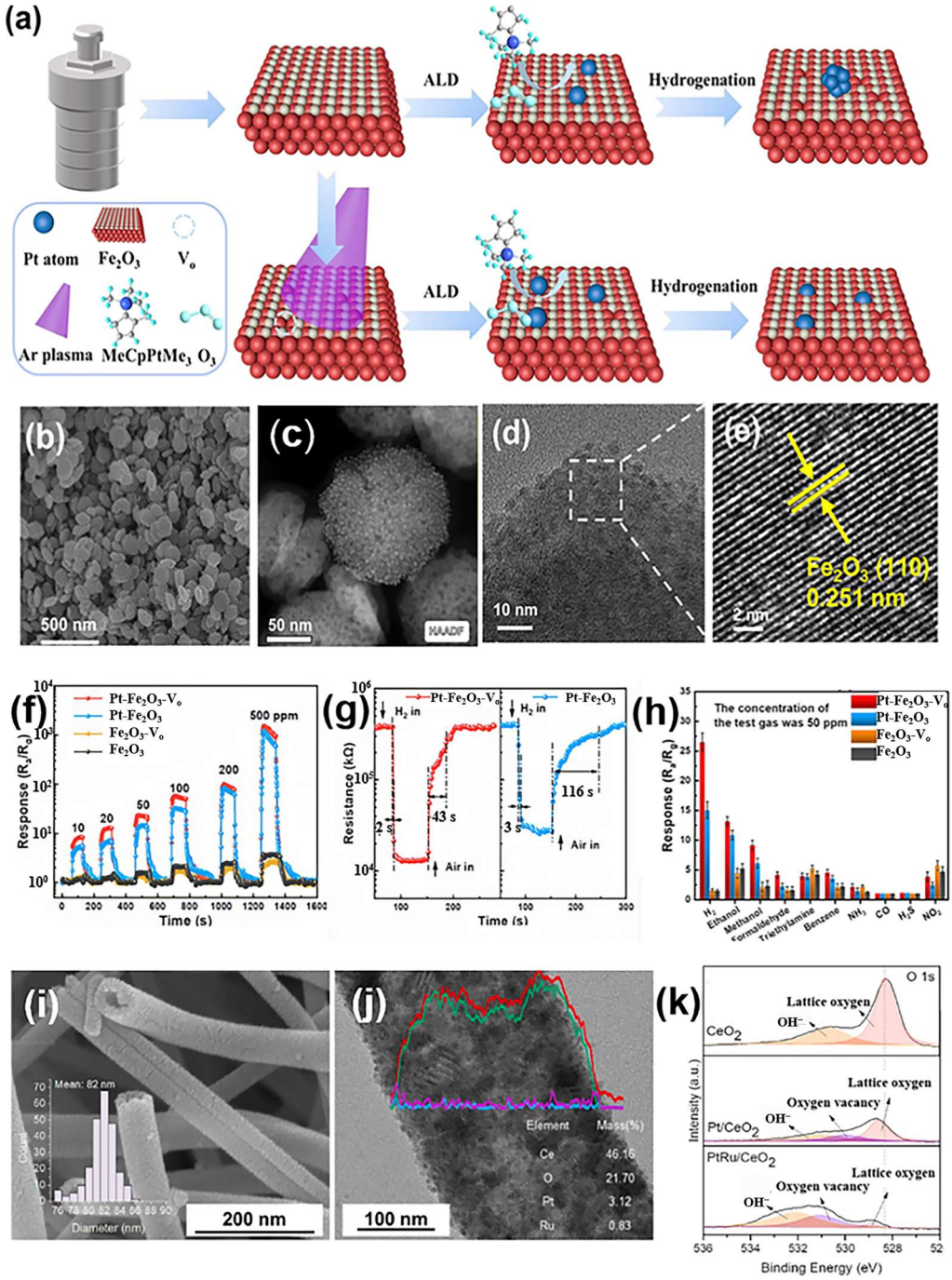

Figure 10. (**a**) Synthesis of Pt-loaded Fe_2O_3 NSs (Pt–Fe_2O_3–Vo). Characterization of Pt–Fe_2O_3–Vo [85]: (**b**) SEM images [83]; (**c**) EDX elemental mappings [83]; (**d**,**e**) HRTEM images [83]. (**f**) Dynamic curve of sensor response at different H_2 concentrations [83]. (**g**) Response–recovery time of Pt–Fe_2O_3–Vo and Pt–Fe_2O_3 sensors to 50 ppm of H_2 at 240 °C [83]. (**h**) Selectivity of the sensors to different gases [83]. Reprinted with permission from [83]. Copyright {2024} American Chemical Society. (**i**) FESEM image of Ce electrospun fiber after calcination at 500 °C with inset showing diameter distribution (mean: 82 nm) [84]. (**j**) HRTEM image of PtRu/CeO_2 with energy dispersive spectroscopy mapping [84]. (**k**) X-ray photoelectron spectroscopy of O 1s [84]. Reprinted with permission from Elsevier, copyright 2024.

3.2.3. Other Noble-Metal-Decorated MOSs

In addition to Pd and Pt, other noble-metal-decorated MOS nanomaterials also exhibit excellent H_2 sensing performance, such as Au, Ag, Ir, etc.

Hyodo et al. [114] fabricated Au(n)/Pt/TiO_2 for H_2 sensing. They found that water molecules and/or hydroxyl groups adsorbed on the surface played a crucial role in increasing the H_2 adsorption and dissociation on the surface, thereby enhancing H_2 sensing performances.

Shao et al. (Table 1) [85] introduced a novel H_2 sensor featuring a sandwich structure that incorporates Ag. This structure comprises a catalytic sensitization layer composed of Ag NPs, a gas sensing layer of SnO_2, and an electron supply layer of graphitic carbon nitride (g-C_3N_4), collectively referred to as the catalytic-sensitization-layer gas-sensing-layer electron-supply-layer (CSE) configuration (Figure 11a). The optimal Ag@SnO_2@g-C_3N_4 material exhibited a detection limit of 30 ppb, with response and recovery times of 7 s and 9.7 s, respectively, as well as remarkable long-term stability. Guo et al. (Table 1) [86] achieved successful redispersion of Ir NPs through carbon-assisted pyrolysis, thereby enhancing the activity and stability of H_2 sensors. They used a typical metal–organic framework [115–117], ZIF-8, as the precursor to obtain the carbon-decorated ZnO via the annealing in N_2 and calcination in air (Figure 11b). The obtained materials inherited the porous structure from the ZIF-8 and showed a large specific area, which guaranteed rich reactive sites. By improving the dispersion and uniformity of Ir NPs, the catalytic performance of the material was significantly enhanced. The redispersed Ir NPs possess a larger active surface area, which is pivotal in enhancing the performance of the H_2 sensor.

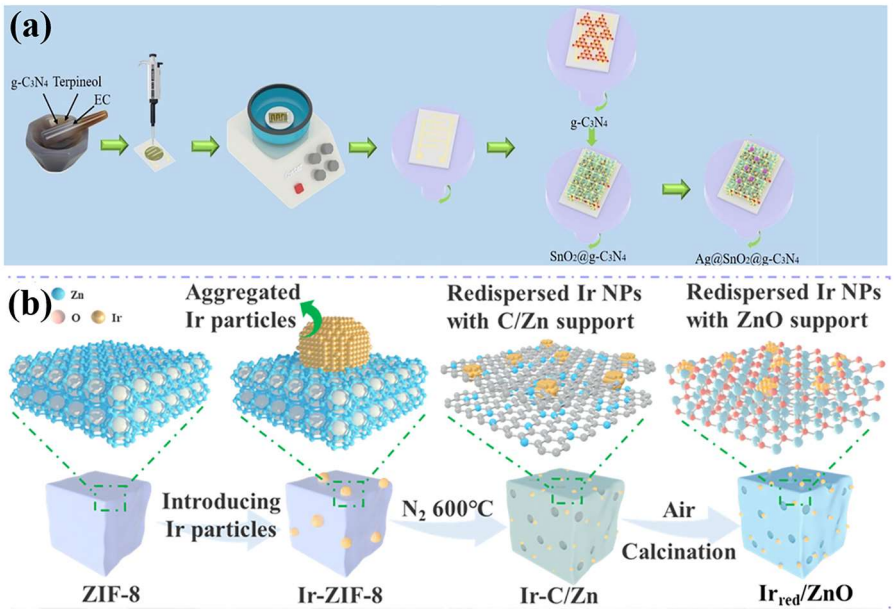

Figure 11. (**a**) Fabrication process of Ag@SnO_2@g-C_3N_4 [85]. Reprinted with permission from Elsevier, copyright 2024. (**b**) Schematic illustration of the Ir_{red}/ZnO synthetic route [86]. Reprinted with permission from [86]. Copyright {2024} American Chemical Society.

4. Conclusions

Chemoresistive H_2 sensors play a pivotal role in various fields, including the hydrogen energy industry, environmental monitoring, and medical diagnosis. The development of cost-effective sensing materials is crucial for advancing these applications. MOSs have emerged as potential candidates for H_2 sensing, yet their inherent sensing performance remains limited. To enhance their performances, the introduction of noble metals to create noble-metal-decorated MOSs sensing materials has become a widely adopted strategy.

Despite recent extensive research and reviews documenting progress in this field, a comprehensive analysis specifically addressing the rational design of sensing materials to optimize the overall performance of noble-metal-decorated MOS-based chemoresistive

H_2 sensors is lacking. This review summarizes the recent research advancements in noble-metal-decorated MOSs-based H_2 sensing materials. We comprehensively consolidate and analyze the strategies utilized in the literature, particularly those reported within the last three years, to furnish a foundational comprehension of the rationale underlying the design of highly efficient chemoresistive H_2 sensors. Current research efforts in this field primarily focus on noble metals such as Pd, Pt, Au, Ag, and Ir, while the MOSs are mainly SnO_2, ZnO, and NiO. Enhancing the dispersion and uniformity of noble metal NPs is anticipated to boost the catalytic properties of these materials. Furthermore, manipulating the morphology of noble-metal-decorated MOSs-based sensing materials is another promising strategy. Morphologies that can yield a high specific surface area, such as NWs [5,58,59], NSs [60], NFs [59], NRs [64], and NTs [66], are preferred due to the abundance of reaction sites. Additionally, the construction of MOSs into heterojunctions, such as p-n-type NiO-Fe_2O_3 and PdO-WO_3, or the incorporation of other components like G and rGO, can further improve the H_2 sensing performance of the material. These strategies collectively offer significant potential for enhancing the sensing capabilities of noble-metal-decorated MOSs in H_2 detection applications.

The incorporation of oxygen vacancies and the precise modulation of their concentrations within MOSs constitute a widely employed strategy. Reducible oxides, exemplified by ZnO, CeO_2, and Fe_2O_3, are typically utilized for this purpose. The creation of oxygen defects is commonly achieved through gas reduction and calcination treatments. However, these methodologies often suffer from complex or dangerous conditions, including high temperatures and reducing atmospheres. Consequently, the development of a safe and easily operated method for controlling oxygen vacancy concentration at RT utilizing an appropriate reducing agent is important. Ascorbic acid has emerged as a promising candidate for facilitating the formation of both surface-bound and intrinsic hydroxyl groups in the context of oxygen vacancy modulation. The adoption of the hydroxyl-oxygen vacancy model for sensing materials heralds a novel approach to synthesizing high-performance gas sensors. Nonetheless, the attainment of remarkably high response values at RT is accompanied by an elongation in the recovery time to the initial baseline. The challenge of reducing recovery time while maintaining high sensor responsiveness remains an area requiring further exploration and investigation.

The H_2 sensing performances of perovskite materials such as $BaTiO_3$, which are also prone to oxygen vacancies, have not been widely explored like materials such as SnO_2 and WO_3, despite their physical and chemical properties making them interesting candidates for gas sensing applications [118]. Perhaps due to its complex H_2 sensing mechanism, it may undergo a phase transition from ferroelectric to paraelectric within the temperature range of H_2 sensing. Multiple influencing factors make it complex to regulate their H_2 sensing performances. Fully understanding the H_2 sensing mechanism of such systems can help improve the H_2 sensing performance of such materials.

Multi-sensing mode represents one of the most promising avenues for future development in gas sensing technology. Gas sensors equipped with a single sensing mode are frequently constrained by their operational principles and the properties of sensitive materials, potentially leading to false positives or negatives in specific conditions. By integrating sensors based on diverse principles, such as electrochemical, optical, thermal, and chemical impedance [119], the multi-sensing mode facilitates multi-dimensional detection of target gases. This integration significantly enhances detection accuracy and reliability, mitigating the risks associated with false positives and negatives. For instance, combining the gasochromic properties of WO_3 with the chemoresistive characteristics of SnO_2 enables the design of an H_2 sensor with a dual detection mode, thereby improving its detection accuracy and reliability. Furthermore, under the multi-sensing mode, algorithms such as

machine learning [120] can be employed to process and analyze this data by amalgamating multiple sensors and gathering extensive data [121–125], enabling precise predictions of gas concentration and real-time detection under complex environments.

Although chemoresistive H_2 sensors based on noble-metal-decorated MOSs have demonstrated their high responsiveness and low detection limits, they also face many challenges, such as performance issues in high-temperature environments, poor selectivity, and humidity-dependent response. Breakthroughs on these issues are needed in the future.

In summary, the future development of noble-metal-decorated MOSs-based H_2 sensors may follow the directions of cost-effectiveness, intelligence, and integration.

Author Contributions: Conceptualization, X.S. and S.X.; validation, H.Z., S.Z., H.Y. and M.Z.; formal analysis, M.Z., H.Z., S.Z. and H.Y.; investigation, S.Z., M.Z., H.Z. and H.Y.; resources, S.Z., H.Y., M.Z. and X.S.; data curation, S.Z., H.Z. and H.Y.; writing—original draft preparation, M.Z.; writing—review and editing, X.S. and S.X.; supervision, X.S. and S.X.; project administration, X.S. and S.X.; funding acquisition, X.S. and S.X. All authors have read and agreed to the published version of the manuscript.

Funding: This work was financially supported by the Natural Science Foundation of Shanghai (23ZR1425500) and Class III Peak Discipline of Shanghai—Materials Science and Engineering (High-Energy Beam Intelligent Processing and Green Manufacturing).

Institutional Review Board Statement: Not applicable.

Informed Consent Statement: Not applicable.

Data Availability Statement: The original contributions presented in this study are included in the article material. Further inquiries can be directed to the corresponding authors.

Acknowledgments: The authors are very grateful to Shanghai Science and Technology Commission for the support.

Conflicts of Interest: The authors declare no conflicts of interest.

References

1. Lin, T.-C.; Wu, J.-Y.; Mendez, A.J.J.; Salazar, N.; Hsu, H.-L.; Huang, W.-C. A Study of MgZnO Thin Film for Hydrogen Sensing Application. *Materials* **2024**, *17*, 3677. [CrossRef] [PubMed]
2. Sisman, O.; Zappa, D.; Maraloiu, V.-A.; Comini, E. Fabrication of CuO (p)–ZnO (n) Core–Shell Nanowires and Their H_2-Sensing Properties. *Materials* **2023**, *16*, 4802. [CrossRef] [PubMed]
3. Alkhabet, M.M.; Yaseen, Z.M.; Eldirderi, M.M.A.; Khedher, K.M.; Jawad, A.H.; Girei, S.H.; Salih, H.K.; Paiman, S.; Arsad, N.; Mahdi, M.A.; et al. Palladium/Graphene Oxide Nanocomposite for Hydrogen Gas Sensing Applications Based on Tapered Optical Fiber. *Materials* **2022**, *15*, 8167. [CrossRef]
4. Yuan, S.; Zeng, S.; Hu, Y.; Kong, W.; Yang, H.; Gong, P.; Xiao, T.; Wang, H.; Wan, H.; Li, Q.; et al. Epitaxial Metal–Organic Framework-Mediated Electron Relay for H_2 Detection on Demand. *ACS Nano* **2024**, *18*, 19723–19731. [CrossRef] [PubMed]
5. Zhao, M.; Nitta, R.; Izawa, S.; Yamaura, J.; Majima, Y. Nano-Patterned CuO Nanowire Nanogap Hydrogen Gas Sensor with Voids. *Adv. Funct. Mater.* **2024**, 2415971. [CrossRef]
6. Shooshtari, M. Ammonia Gas Sensors Based on Multi-Wall Carbon Nanofiber Field Effect Transistors by Using Gate Modulation. *Colloids Surf. A Physicochem. Eng. Asp.* **2025**, *704*, 135563. [CrossRef]
7. Galvani, M.; Freddi, S.; Sangaletti, L. Disclosing Fast Detection Opportunities with Nanostructured Chemiresistor Gas Sensors Based on Metal Oxides, Carbon, and Transition Metal Dichalcogenides. *Sensors* **2024**, *24*, 584. [CrossRef] [PubMed]
8. Zeng, C.; Lu, N.; Wen, Y.; Liu, G.; Zhang, R.; Zhang, J.; Wang, F.; Liu, X.; Li, Q.; Tang, Z.; et al. Engineering Nanozymes Using DNA for Catalytic Regulation. *ACS Appl. Mater. Interfaces* **2019**, *11*, 1790–1799. [CrossRef]
9. Kafil, V.; Sreenan, B.; Hadj-Nacer, M.; Wang, Y.; Yoon, J.; Greiner, M.; Chu, P.; Wang, X.; Fadali, M.S.; Zhu, X. Review of Noble Metal and Metal-Oxide-Semiconductor Based Chemiresistive Hydrogen Sensors. *Sens. Actuators A Phys.* **2024**, *373*, 115440. [CrossRef]
10. Sharma, B.; Sharma, A.; Kim, J.-S. Recent Advances on H_2Sensor Technologies Based on MOX and FET Devices: A Review. *Sens. Actuators B Chem.* **2018**, *262*, 758–770. [CrossRef]

11. Kamal Hossain, M.; Ahmed Drmosh, Q. Noble Metal-Decorated Nanostructured Zinc Oxide: Strategies to Advance Chemiresistive Hydrogen Gas Sensing. *Chem. Rec.* **2022**, *22*, e202200090. [CrossRef] [PubMed]
12. LaConti, A.B.; Maget, H.J.R. Electrochemical Detection of H_2, CO, and Hydrocarbons in Inert or Oxygen Atmospheres. *J. Electrochem. Soc.* **1971**, *118*, 506. [CrossRef]
13. Ghosh, P.; Huang, M. Effects of Strain on Various Properties and Applications on One-Dimensional Nano-/Microstructures. *J. Mater. Sci.* **2020**, *55*, 7208–7225. [CrossRef]
14. McAleer, J.F.; Moseley, P.t.; Bourke, P.; Norris, J.O.W.; Stephan, R. Tin Dioxide Gas Sensors: Use of the Seebeck Effect. *Sens. Actuators* **1985**, *8*, 251–257. [CrossRef]
15. Zhang, W.; Zou, J.; Sun, J.; Wang, W.; Shan, L.; Bao, K.; Gao, W.; Zhou, Y.; Jin, Q.; Jian, J. Fabrication and Sensing Performance of Carrier-Free Catalytic Combustion Hydrogen Sensors Based on Electrodeposition Method. *Int. J. Hydrogen Energy* **2024**, *61*, 1356–1364. [CrossRef]
16. Butler, M.A. Optical Fiber Hydrogen Sensor. *Appl. Phys. Lett.* **1984**, *45*, 1007–1009. [CrossRef]
17. Shen, C.; Xie, Z.; Huang, Z.; Yan, S.; Sui, W.; Zhou, J.; Wang, Z.; Han, W.; Zeng, X. Review of the Status and Prospects of Fiber Optic Hydrogen Sensing Technology. *Chemosensors* **2023**, *11*, 473. [CrossRef]
18. Seiyama, T.; Kato, A.; Fujiishi, K.; Nagatani, M. A New Detector for Gaseous Components Using Semiconductive Thin Films. *Anal. Chem.* **1962**, *34*, 1502–1503. [CrossRef]
19. Cai, Z.; Park, S. Improved SnO_2 Nanowire Acetone Sensor with Uniform Co_3O_4 Nanoparticle Decoration. *J. Environ. Chem. Eng.* **2023**, *11*, 111504. [CrossRef]
20. Li, R.; Chen, S.; Lou, Z.; Li, L.; Huang, T.; Song, Y.; Chen, D.; Shen, G. Fabrication of Porous SnO_2 Nanowires Gas Sensors with Enhanced Sensitivity. *Sens. Actuators B Chem.* **2017**, *252*, 79–85. [CrossRef]
21. Mahendraprabhu, K.; Selva Sharma, A.; Elumalai, P. CO Sensing Performances of YSZ-Based Sensor Attached with Sol-Gel Derived ZnO Nanospheres. *Sens. Actuators B Chem.* **2019**, *283*, 842–847. [CrossRef]
22. Cao, Y.; Zhong, H.; Chen, B.; Lin, X.; Shen, J.; Ye, M. Liquid Metal-Assisted Hydrothermal Preparation of Cobalt Disulfide on the Polymer Tape Surface for Flexible Sensor. *Nano Res.* **2023**, *16*, 7575–7582. [CrossRef]
23. Prete, P.; Lovergine, N.; Tapfer, L. Nanostructure Size Evolution during Au-Catalysed Growth by Carbo-Thermal Evaporation of Well-Aligned ZnO Nanowires on (100)Si. *Appl. Phys. A* **2007**, *88*, 21–26. [CrossRef]
24. Kabitakis, V.; Gagaoudakis, E.; Moschogiannaki, M.; Kiriakidis, G.; Seitkhan, A.; Firdaus, Y.; Faber, H.; Yengel, E.; Loganathan, K.; Deligeorgis, G.; et al. A Low-Power CuSCN Hydrogen Sensor Operating Reversibly at Room Temperature. *Adv. Funct. Mater.* **2022**, *32*, 2102635. [CrossRef]
25. Huang, Z.; Xu, S.; Zhang, Z.; Wang, Z.; Si, M.; Hu, Y. Strain and Defect Engineering of High-Performance Monolayer Two-Dimensional Material/Ag Nanoparticles Optoelectronic FET Sensor through Multiple Laser Shock. *Sens. Actuators B Chem.* **2024**, *413*, 135856. [CrossRef]
26. Zhao, C.; Wu, H. A First-Principles Study on the Interaction of Biogas with Noble Metal (Rh, Pt, Pd) Decorated Nitrogen Doped Graphene as a Gas Sensor: A DFT Study. *Appl. Surf. Sci.* **2018**, *435*, 1199–1212. [CrossRef]
27. Michalzik, M.; Wilke, R.; Büttgenbach, S. Miniaturized QCM-Based Flow System for Immunosensor Application in Liquid. *Sens. Actuators B Chem.* **2005**, *111–112*, 410–415. [CrossRef]
28. Moon, H.; Park, B.; Hong, D.; Park, K.-S.; Lee, S.; Kim, S. 3D-Structured Soft Bioelectronic Devices with Crack-Free Metal Patterns. *Sens. Actuators B Chem.* **2021**, *343*, 130123. [CrossRef]
29. Lupan, O.; Postica, V.; Wolff, N.; Su, J.; Labat, F.; Ciofini, I.; Cavers, H.; Adelung, R.; Polonskyi, O.; Faupel, F.; et al. Low-Temperature Solution Synthesis of Au-Modified ZnO Nanowires for Highly Efficient Hydrogen Nanosensors. *ACS Appl. Mater. Interfaces* **2019**, *11*, 32115–32126. [CrossRef]
30. Koo, W.-T.; Qiao, S.; Ogata, A.F.; Jha, G.; Jang, J.-S.; Chen, V.T.; Kim, I.-D.; Penner, R.M. Accelerating Palladium Nanowire H_2 Sensors Using Engineered Nanofiltration. *ACS Nano* **2017**, *11*, 9276–9285. [CrossRef]
31. Zhang, S.; Zhang, H.; Yao, H.; Wang, P.; Zhu, M.; Shi, X.; Xu, S. Recent Advances in Metal Oxide Semiconductor Heterojunctions for the Detection of Volatile Organic Compounds. *Chemosensors* **2024**, *12*, 244. [CrossRef]
32. Qiu, T.; Zhou, S.; Ji, J.; Wu, G.; Yan, W.; Ling, M.; Liang, C. High Performance H_2 Sensor Based on RGO-Wrapped SnO_2–Pd Porous Hollow Spheres. *Ceram. Int.* **2022**, *48*, 15056–15063. [CrossRef]
33. Wu, Z.; Wang, Y.; Wu, Q.; Cheng, X.; Wang, Q.; Yang, Y.; An, B.; Wang, P.; Xie, E. SnO_2 Grains with Abundant Surface Oxygen Vacancies for the Ultra-Sensitive Detection of NO_2 at Low Temperature. *Appl. Surf. Sci.* **2023**, *614*, 156223. [CrossRef]
34. Kwon, G.; Kota, A.; Li, Y.; Sohani, A.; Mabry, J.M.; Tuteja, A. On-Demand Separation of Oil-Water Mixtures. *Adv. Mater.* **2012**, *24*, 3666–3671. [CrossRef] [PubMed]
35. Liu, Y.; Lei, Y.; Mao, X.; Qian, H.; Wen, H.-M.; Xia, S.; Xiang, Y.; Chen, Q.; Xie, B.; Hu, J. Wide-Concentration-Range Hydrogen Sensing Using Palladium-Loaded SnO_2 Nanoparticle Films and Understanding of Hydrogen Concentration-Dependent Sensing Mechanism. *Int. J. Hydrogen Energy* **2024**, *62*, 783–793. [CrossRef]

36. Zhu, L.-Y.; Ou, L.-X.; Mao, L.-W.; Wu, X.-Y.; Liu, Y.-P.; Lu, H.-L. Advances in Noble Metal-Decorated Metal Oxide Nanomaterials for Chemiresistive Gas Sensors: Overview. *Nanomicro Lett.* **2023**, *15*, 89. [CrossRef] [PubMed]
37. Sun, C.; Zhang, S.; Wang, P.; Wei, M.; Wang, S.; Shi, X.-R. High-Throughput Screening of Efficient Graphdiyne Supported Transition Metal Single Atom toward Water Electrolysis and Oxygen Reduction. *J. Catal.* **2024**, *439*, 115773. [CrossRef]
38. Zhang, Z.; Luo, L.; Zhang, Y.; Lv, G.; Luo, Y.; Duan, G. Wafer-Level Manufacturing of MEMS H_2 Sensing Chips Based on Pd Nanoparticles Modified SnO_2 Film Patterns. *Adv. Sci.* **2023**, *10*, 2302614. [CrossRef]
39. Kolmakov, A.; Klenov, D.O.; Lilach, Y.; Stemmer, S.; Moskovits, M. Enhanced Gas Sensing by Individual SnO_2 Nanowires and Nanobelts Functionalized with Pd Catalyst Particles. *Nano Lett.* **2005**, *5*, 667–673. [CrossRef]
40. Nakatsuji, H.; Hada, M. Interaction of a Hydrogen Molecule with Palladium. *J. Am. Chem. Soc.* **1985**, *107*, 8264–8266. [CrossRef]
41. Kadhim, I.H.; Hassan, H.A.; Abdullah, Q.N. Hydrogen Gas Sensor Based on Nanocrystalline SnO_2 Thin Film Grown on Bare Si Substrates. *Nanomicro Lett.* **2016**, *8*, 20–28. [CrossRef] [PubMed]
42. Tsang, S.C.; Bulpitt, C.D.A.; Mitchell, P.C.H.; Ramirez-Cuesta, A.J. Some New Insights into the Sensing Mechanism of Palladium Promoted Tin (IV) Oxide Sensor. *J. Phys. Chem. B* **2001**, *105*, 5737–5742. [CrossRef]
43. Mirzaei, A.; Yousefi, H.R.; Falsafi, F.; Bonyani, M.; Lee, J.-H.; Kim, J.-H.; Kim, H.W.; Kim, S.S. An Overview on How Pd on Resistive-Based Nanomaterial Gas Sensors Can Enhance Response toward Hydrogen Gas. *Int. J. Hydrogen Energy* **2019**, *44*, 20552–20571. [CrossRef]
44. Lupan, O.; Postica, V.; Hoppe, M.; Wolff, N.; Polonskyi, O.; Pauporté, T.; Viana, B.; Majérus, O.; Kienle, L.; Faupel, F.; et al. PdO/PdO_2 Functionalized ZnO : Pd Films for Lower Operating Temperature H_2 Gas Sensing. *Nanoscale* **2018**, *10*, 14107–14127. [CrossRef] [PubMed]
45. Marikutsa, A.; Rumyantseva, M.; Gaskov, A. Specific Interaction of PdO_{x-} and RuO_{y-} Modified Tin Dioxide with CO and NH_3 Gases: Kelvin Probe and DRIFT Studies. *J. Phys. Chem. C* **2015**, *119*, 24342–24350. [CrossRef]
46. Kim, H.; Pak, Y.; Jeong, Y.; Kim, W.; Kim, J.; Jung, G.Y. Amorphous Pd-Assisted H_2 Detection of ZnO Nanorod Gas Sensor with Enhanced Sensitivity and Stability. *Sens. Actuators B Chem.* **2018**, *262*, 460–468. [CrossRef]
47. Meng, X.; Bi, M.; Xiao, Q.; Gao, W. Ultrasensitive Gas Sensor Based on $Pd/SnS_2/SnO_2$ Nanocomposites for Rapid Detection of H_2. *Sens. Actuators B Chem.* **2022**, *359*, 131612. [CrossRef]
48. Kim, J.-H.; Mirzaei, A.; Kim, H.W.; Kim, S.S. Improving the Hydrogen Sensing Properties of SnO_2 Nanowire-Based Conductometric Sensors by Pd-Decoration. *Sens. Actuators B Chem.* **2019**, *285*, 358–367. [CrossRef]
49. Chen, C.; Chen, W.; Liu, Q.; Liu, Y.; Xiao, G.; Chen, C.; Li, F.; Zhou, J. Electrospinning of Pd–In_2O_3 Nanofibers for High-Performance Room Temperature Hydrogen Sensors. *ACS Appl. Nano Mater.* **2022**, *5*, 12646–12655. [CrossRef]
50. Cai, Z.; Park, S. Synthesis of Pd Nanoparticle-Decorated SnO_2 Nanowires and Determination of the Optimum Quantity of Pd Nanoparticles for Highly Sensitive and Selective Hydrogen Gas Sensor. *Sens. Actuators B Chem.* **2020**, *322*, 128651. [CrossRef]
51. Jiang, P.; Kang, L.; Zheng, X.; Zeng, Z.; Sanvito, S. Computational Prediction of a Two-Dimensional Semiconductor SnO_2 with Negative Poisson's Ratio and Tunable Magnetism by Doping. *Phys. Rev. B* **2020**, *102*, 195408. [CrossRef]
52. Khan, I.; Yamani, Z.H.; Qurashi, A. Sonochemical-Driven Ultrafast Facile Synthesis of SnO_2 Nanoparticles: Growth Mechanism Structural Electrical and Hydrogen Gas Sensing Properties. *Ultrason. Sonochem* **2017**, *34*, 484–490. [CrossRef]
53. Cingolani, R.; Di Dio, M.; Lomascolo, M.; Rinaldi, R.; Prete, P.; Vasanelli, L.; Vanzetti, L.; Bassani, F.; Bonanni, A.; Sorba, L.; et al. Photocurrent Spectroscopy of $Zn_{1-x}Cd_x/ZnSe$ Quantum Wells in p-i-n Heterostructures. *Phys. Rev. B* **1994**, *50*, 12179–12182. [CrossRef] [PubMed]
54. Huang, S.; Shi, X.-R.; Sun, C.; Zhang, X.; Huang, M.; Liu, R.; Wang, H.; Xu, S. Template-Controlled in-Situ Growing of NiCo-MOF Nanosheets on Ni Foam with Mixed Linkers for High Performance Asymmetric Supercapacitors. *Appl. Surf. Sci.* **2022**, *572*, 151344. [CrossRef]
55. Zhang, X.; Shi, X.; Wang, P.; Bao, Z.; Huang, M.; Xu, Y.; Xu, S. Bio-Inspired Design of NiFeP Nanoparticles Embedded in (N, P) Co-Doped Carbon for Boosting Overall Water Splitting. *Dalton Trans.* **2023**, *52*, 6860–6869. [CrossRef] [PubMed]
56. Duan, Z.; Shi, X.-R.; Sun, C.; Lin, W.; Huang, S.; Zhang, X.; Huang, M.; Yang, Z.; Xu, S. Interface Engineered Hollow Co_3O_4@$CoNi_2S_4$ Nanostructure for High Efficiency Supercapacitor and Hydrogen Evolution. *Electrochim. Acta* **2022**, *412*, 140139. [CrossRef]
57. Cao, F.; Shi, X.-R.; Wang, P.; Zhao, W.; Huang, M.; Hu, J.; Xu, S.; Zhao, G. Multistage Interface Engineered Cobalt Polysulfides Core-Shell Nanostructures for Dual Energy Storage Devices and Hydrogen Evolution. *Vacuum* **2023**, *216*, 112461. [CrossRef]
58. Li, G.; Shen, Y.; Zhao, S.; Li, A.; Zhao, T.; Tang, C.; Yan, C.; Gao, S.; Yuan, Z.; Meng, F. Detection of Ppm-Level H_2 via RGO-SnO_2-ZnO Nanocomposites: Considering Compositional Matching in Designing Heterostructured Gas-Sensing Materials. *Sens. Actuators B Chem.* **2023**, *396*, 134560. [CrossRef]
59. Kim, K.-H.; Jo, M.-S.; Kim, S.-H.; Kim, B.; Kang, J.; Yoon, J.-B.; Seo, M.-H. Long-Term Reliable Wireless H_2 Gas Sensor via Repeatable Thermal Refreshing of Palladium Nanowire. *Nat. Commun.* **2024**, *15*, 8761. [CrossRef] [PubMed]
60. Li, G.; Du, K.; Wang, X.; Wang, X.; Chen, B.; Qiu, C.; Xu, J. Pd Nanoparticles Decorated SnO_2 Ultrathin Nanosheets for Highly Sensitive H_2 Sensor: Experimental and Theoretical Studies. *Int. J. Hydrogen Energy* **2024**, *50*, 761–771. [CrossRef]

61. Badie, C.; Mirzaei, A.; Lee, J.; Sayegh, S.; Bechelany, M.; Santinacci, L.; Kim, H.W.; Kim, S.S. Selective Detection of H_2 Gas in Gas Mixtures Using NiO-Shelled Pd-Decorated ZnO Nanowires. *Adv. Mater. Technol.* **2024**, *9*, 2302801. [CrossRef]
62. Tang, M.; Qin, C.; Sun, X.; Li, M.; Wang, Y.; Cao, J.; Wang, Y. Enhanced H_2 Gas Sensing Performances by Pd-Loaded In_2O_3 Microspheres. *Appl. Phys. A* **2024**, *130*, 741. [CrossRef]
63. Wang, Y.; Wang, Y.; Sun, X.; Li, M.; Tang, M.; Cao, J.; Qin, C. Enhanced H_2 Sensing Performance of Pd-Modified ZnO Nanorods under Visible Light Excitation. *Int. J. Hydrogen Energy* **2024**, *50*, 1470–1479. [CrossRef]
64. Yang, X.-Y.; Chen, H.-N.; Yue, L.-J.; Gong, F.-L.; Xie, K.-F.; Wei, S.-Z.; Zhang, Y.-H. Surface Engineering of 1D Na-Doped Pd/WO_3 Nanorods for Chemiresistive H_2 Sensing. *Sens. Actuators B Chem.* **2025**, *423*, 136825. [CrossRef]
65. Tasyurek, L.B.; Isik, E.; Isik, I.; Kilinc, N. Enhancing the Performance of TiO_2 Nanotube-Based Hydrogen Sensors through Crystal Structure and Metal Electrode. *Int. J. Hydrogen Energy* **2024**, *54*, 678–690. [CrossRef]
66. Chen, C.; Wang, Y.; Xiao, G.; Chen, C.; He, X.; Zhou, J.; Le, J.; Zhou, X. Hydrogen-Sensitive Properties of Fern-like In_2O_3@ZnO@Pd Nanotubes at Room Temperature. *Int. J. Hydrogen Energy* **2024**, *88*, 395–406. [CrossRef]
67. Nam, G.B.; Eom, T.H.; Cho, S.H.; Kim, Y.J.; Choi, S.; Cheon, W.S.; Park, S.J.; Shokouhimehr, M.; Suh, J.M.; Ryu, J.-E.; et al. Maximized Nanojunctions in Pd/SnO_2 Nanoparticles for Ultrasensitive and Rapid H_2 Detection. *Chem. Eng. J.* **2024**, *494*, 153116. [CrossRef]
68. Escobar-Chávez, J.J.; López-Cervantes, M.; Naïk, A.; Kalia, Y.N.; Quintanar-Guerrero, D.; Ganem-Quintanar, A. Applications of Thermo-Reversible Pluronic F-127 Gels in Pharmaceutical Formulations. *J. Pharm. Pharm. Sci.* **2006**, *9*, 339–358. [PubMed]
69. Potyrailo, R.A. Multivariable Sensors for Ubiquitous Monitoring of Gases in the Era of Internet of Things and Industrial Internet. *Chem. Rev.* **2016**, *116*, 11877–11923. [CrossRef] [PubMed]
70. Nguyen, T.T.D.; Van Dao, D.; Kim, D.-S.; Lee, H.-J.; Oh, S.-Y.; Lee, I.-H.; Yu, Y.-T. Effect of Core and Surface Area toward Hydrogen Gas Sensing Performance Using Pd@ZnO Core-Shell Nanoparticles. *J. Colloid. Interface Sci.* **2021**, *587*, 252–259. [CrossRef] [PubMed]
71. Cai, Z.; Park, J.; Park, S. Synergistic Effect of Pd and Fe_2O_3 Nanoparticles Embedded in Porous NiO Nanofibers on Hydrogen Gas Detection: Fabrication, Characterization, and Sensing Mechanism Exploration. *Sens. Actuators B Chem.* **2023**, *388*, 133836. [CrossRef]
72. Zhu, S.; Tian, Q.; Wu, G.; Bian, W.; Sun, N.; Wang, X.; Li, C.; Zhang, Y.; Dou, H.; Gong, C.; et al. Highly Sensitive and Stable H_2 Gas Sensor Based on p-PdO-n-WO_3-Heterostructure-Homogeneously-Dispersing Thin Film. *Int. J. Hydrogen Energy* **2022**, *47*, 17821–17834. [CrossRef]
73. Yin, X.-T.; Yang, Z.-Y.; Dastan, D.; Liu, Y.; Tan, X.-M.; Gao, X.-C.; Zhou, Y.-W.; Li, J.; Ma, X.-G. Sensitivity and Selectivity Pt Loaded SnO_2–Co_3O_4 Gas Sensor for Hydrogen Detection. *Ceram. Int.* **2023**, *49*, 38717–38725. [CrossRef]
74. Zhang, X.; Sun, J.; Tang, K.; Wang, H.; Chen, T.; Jiang, K.; Zhou, T.; Quan, H.; Guo, R. Ultralow Detection Limit and Ultrafast Response/Recovery of the H_2 Gas Sensor Based on Pd-Doped RGO/ZnO-SnO_2 from Hydrothermal Synthesis. *Microsyst. Nanoeng.* **2022**, *8*, 67. [CrossRef]
75. Song, Y.; Meng, X.; Bi, M.; Gao, W. Conductometric H_2 Sensors at Room Temperature Based on Palladium Nanoparticles on Ceria. *Sens. Actuators B Chem.* **2023**, *375*, 132957. [CrossRef]
76. Luo, Y.; Zhang, C. Pt-Activated TiO_2-MoS_2 Nanocomposites for H_2 Detection at Low Temperature. *J. Alloys Compd.* **2018**, *747*, 550–557. [CrossRef]
77. Huang, Y.; Chen, F.; Meng, L.; Hu, Y.; Chen, W. Aging and Activation of Room Temperature Hydrogen Sensitive Pt–SnO_2 Composite Nanoceramics. *J. Mater. Sci.* **2022**, *57*, 15267–15275. [CrossRef]
78. Zhu, S.; Li, P.; Wu, G.; Li, Z.; Wu, P.; Hu, Y.; Gu, H.; Chen, W. Extraordinary Room-Temperature Hydrogen Sensing Capabilities with High Humidity Tolerance of Pt SnO_2 Composite Nanoceramics Prepared Using SnO_2 Agglomerate Powder. *Int. J. Hydrogen Energy* **2018**, *43*, 21177–21185. [CrossRef]
79. Uddin, M.M.; Rahaman, M.H.; Kim, H.C. Highly Stable Hydrogen Sensing Properties of Pt–ZnO Nanoparticle Layers Deposited on an Alumina Substrate for High-Temperature Industrial Applications. *Sens. Actuators B Chem.* **2022**, *368*, 132088. [CrossRef]
80. Tan, T.; Hang, Z.; Li, X.; Wang, S.; Homewood, K.; Xia, X.; Bao, Y.; Gao, Y. Ultra-High-Response Heat Free H_2 Sensor Based on a WO_3/Pt-ZnO Thin Film. *J. Alloys Compd.* **2024**, *979*, 173527. [CrossRef]
81. Kathiravan, D.; Huang, B.-R.; Saravanan, A. Self-Assembled Hierarchical Interfaces of ZnO Nanotubes/Graphene Heterostructures for Efficient Room Temperature Hydrogen Sensors. *ACS Appl. Mater. Interfaces* **2017**, *9*, 12064–12072. [CrossRef]
82. Vivekanandan, A.K.; Huang, B.-R.; Kathiravan, D.; Saravanan, A.; Prasannan, A.; Tsai, H.-C.; Chen, S.-H. Effect of MoS_2 Solution on Reducing the Wall Thickness of ZnO Nanotubes to Enhance Their Hydrogen Gas Sensing Properties. *J. Alloys Compd.* **2021**, *854*, 157102. [CrossRef]
83. Zhang, S.; Chang, X.; Zhou, L.; Liu, X.; Zhang, J. Stabilizing Single-Atom Pt on Fe_2O_3 Nanosheets by Constructing Oxygen Vacancies for Ultrafast H_2 Sensing. *ACS Sens.* **2024**, *9*, 2101–2109. [CrossRef] [PubMed]
84. Kim, J.Y.; Jang, B.; Lim, M.; Park, J.Y.; Choa, Y.-H. Enhanced PtRu by CeO_2 Hollow Nanofibers: Hydrogen Gas Sensing with CO-Resistant in Fuel Cell. *J. Power Sources* **2024**, *613*, 234842. [CrossRef]

85. Shao, X.; Zhang, D.; Tang, M.; Zhang, H.; Wang, Z.; Jia, P.; Zhai, J. Amorphous Ag Catalytic Layer-SnO_2 Sensitive Layer-Graphite Carbon Nitride Electron Supply Layer Synergy-Enhanced Hydrogen Gas Sensor. *Chem. Eng. J.* **2024**, *495*, 153676. [CrossRef]
86. Guo, M.; Li, X.; Wang, L.; Xue, Z.; Xu, J. Redispersing Ir Nanoparticles via a Carbon-Assisted Pyrolysis Process to Break the Activity–Stability Trade-Off of H_2 Sensors. *ACS Sens.* **2024**, *9*, 3327–3337. [CrossRef]
87. Zhang, Y.-W.; Liu, W.-S.; Chen, J.-S.; Niu, H.-L.; Mao, C.-J.; Jin, B.-K. Metal-Organic Gel and Metal-Organic Framework Based Switchable Electrochemiluminescence RNA Sensing Platform for Zika Virus. *Sens. Actuators B Chem.* **2020**, *321*, 128456. [CrossRef]
88. Skála, T.; Veltruská, K.; Moroseac, M.; Matolınová, I.; Korotchenkov, G.; Matolın, V. Study of Pd–In Interaction during Pd Deposition on Pyrolytically Prepared In_2O_3. *Appl. Surf. Sci.* **2003**, *205*, 196–205. [CrossRef]
89. Ramanathan, R.; Nagarajan, S.; Jamdhar, S.; Barshilia, H.C.; Mallik, R.C. Interface Surface Effect of SnO_2–GO Thin-Film Heterostructure on H_2 Gas Sensor Performance. *ACS Appl. Electron. Mater.* **2024**, *6*, 7832–7846. [CrossRef]
90. Li, S.; Zhao, C.; Zhou, S.; Zhang, Y.; Zhu, P.; Yu, J. Non-Covalent Interaction-Driven Self-Assembly of Perylene Diimide on RGO for Room-Temperature Sensing of Triethylamine with Enhanced Immunity to Humidity. *Chem. Eng. J.* **2020**, *385*, 123397. [CrossRef]
91. Degler, D.; Weimar, U.; Barsan, N. Current Understanding of the Fundamental Mechanisms of Doped and Loaded Semiconducting Metal-Oxide-Based Gas Sensing Materials. *ACS Sens.* **2019**, *4*, 2228–2249. [CrossRef] [PubMed]
92. Lee, J.-H.; Katoch, A.; Choi, S.-W.; Kim, J.-H.; Kim, H.W.; Kim, S.S. Extraordinary Improvement of Gas-Sensing Performances in SnO_2 Nanofibers Due to Creation of Local *p*–*n* Heterojunctions by Loading Reduced Graphene Oxide Nanosheets. *ACS Appl. Mater. Interfaces* **2015**, *7*, 3101–3109. [CrossRef] [PubMed]
93. Wu, H.; Yu, J.; Li, Z.; Yao, G.; Cao, R.; Li, X.; Zhu, H.; He, A.; Tang, Z. Microhotplate Gas Sensors Incorporated with Al Electrodes and 3D Hierarchical Structured PdO/PdO_2-SnO_2:Sb Materials for Sensitive VOC Detection. *Sens. Actuators B Chem.* **2021**, *329*, 128984. [CrossRef]
94. Li, Z.; Liu, X.; Zhou, M.; Zhang, S.; Cao, S.; Lei, G.; Lou, C.; Zhang, J. Plasma-Induced Oxygen Vacancies Enabled Ultrathin ZnO Films for Highly Sensitive Detection of Triethylamine. *J. Hazard. Mater.* **2021**, *415*, 125757. [CrossRef]
95. Cheng, I.-K.; Lin, C.-Y.; Pan, F.-M. Gas Sensing Behavior of ZnO toward H_2 at Temperatures below 300 °C and Its Dependence on Humidity and Pt-Decoration. *Appl. Surf. Sci.* **2021**, *541*, 148551. [CrossRef]
96. Rai, P.; Majhi, S.M.; Yu, Y.-T.; Lee, J.-H. Noble Metal@metal Oxide Semiconductor Core@shell Nano-Architectures as a New Platform for Gas Sensor Applications. *RSC Adv.* **2015**, *5*, 76229–76248. [CrossRef]
97. Kim, H.-J.; Lee, J.-H. Highly Sensitive and Selective Gas Sensors Using P-Type Oxide Semiconductors: Overview. *Sens. Actuators B Chem.* **2014**, *192*, 607–627. [CrossRef]
98. Lee, J.-H.; Kim, J.-Y.; Mirzaei, A.; Kim, H.W.; Kim, S.S. Significant Enhancement of Hydrogen-Sensing Properties of ZnO Nanofibers through NiO Loading. *Nanomaterials* **2018**, *8*, 902. [CrossRef]
99. Song, Z.; Zhang, L.; Zhou, Q.; Zhang, Z.; Dong, Z.; Nie, L.; Liu, Q.; Pan, G. In-Situ Synthesis of Needle-like PdO-Decorated NiO Thin Films on Al_2O_3 Substrates for High-Performance H_2 Sensors. *Ceram. Int.* **2022**, *48*, 31746–31754. [CrossRef]
100. Zhou, S.; Yan, W.; Ling, M.; Liang, C. High-Response H_2 Sensing Performances of ZnO Nanosheets Modulated by Oxygen Vacancies. *Inorg. Chem. Front.* **2023**, *10*, 3255–3262. [CrossRef]
101. Meng, C.; Zhao, G.; Shi, X.-R.; Nie, Q.; Liu, Y.; Lu, Y. Electronic Modulation of $InNi_3C_{0.5}/Fe_3O_4$ by Support Precursor toward Efficient CO_2 Hydrogenation to Methanol. *Appl. Catal. B* **2022**, *316*, 121699. [CrossRef]
102. Meng, C.; Zhao, G.; Shi, X.-R.; Chen, P.; Liu, Y.; Lu, Y. Oxygen-Deficient Metal Oxides Supported Nano-Intermetallic $InNi_3C_{0.5}$ toward Efficient CO_2 Hydrogenation to Methanol. *Sci. Adv.* **2021**, *7*, eabi6012. [CrossRef]
103. Zhu, J.; Zhao, G.; Meng, C.; Chen, P.; Shi, X.-R.; Lu, Y. Superb Ni-Foam-Structured Nano-Intermetallic $InNi_3C_{0.5}$ Catalyst for Hydrogenation of Dimethyl Oxalate to Ethylene Glycol. *Chem. Eng. J.* **2021**, *426*, 130857. [CrossRef]
104. Chen, P.; Zhao, G.; Shi, X.-R.; Zhu, J.; Ding, J.; Lu, Y. Nano-Intermetallic $InNi_3C_{0.5}$ Compound Discovered as a Superior Catalyst for CO_2 Reutilization. *iScience* **2019**, *17*, 315–324. [CrossRef] [PubMed]
105. Si, J.; Zhao, G.; Sun, W.; Liu, J.; Guan, C.; Yang, Y.; Shi, X.-R.; Lu, Y. Oxidative Coupling of Methane: Examining the Inactivity of the MnO_x-Na_2WO_4/SiO_2 Catalyst at Low Temperature. *Angew. Chem. Int. Ed.* **2022**, *61*, e202117201. [CrossRef] [PubMed]
106. Huang, M.; Yao, H.; Cao, F.; Wang, P.; Shi, X.-R.; Zhang, M.; Xu, S. Structural Engineering Evoked Multifunctionality in Molybdate Nanosheets for Industrial Oxygen Evolution and Dual Energy Storage Devices Inspired by Multi-Method Calculations. *J. Colloid. Interface Sci.* **2024**, *676*, 471–484. [CrossRef] [PubMed]
107. Yin, X.-T.; Li, J.; Dastan, D.; Zhou, W.-D.; Garmestani, H.; Alamgir, F.M. Ultra-High Selectivity of H_2 over CO with a p-n Nanojunction Based Gas Sensors and Its Mechanism. *Sens. Actuators B Chem.* **2020**, *319*, 128330. [CrossRef]
108. Yin, X.-T.; Dastan, D.; Gity, F.; Li, J.; Shi, Z.; Alharbi, N.D.; Liu, Y.; Tan, X.-M.; Gao, X.-C.; Ma, X.-G.; et al. Gas Sensing Selectivity of SnO_2-XNiO Sensors for Homogeneous Gases and Its Selectivity Mechanism: Experimental and Theoretical Studies. *Sens. Actuators A Phys.* **2023**, *354*, 114273. [CrossRef]
109. Li, S.; Zhang, Y.; Han, L.; Li, X.; Xu, Y. Highly Sensitive and Selective Triethylamine Gas Sensor Based on Hierarchical Radial CeO_2/ZnO n-n Heterojunction. *Sens. Actuators B Chem.* **2022**, *367*, 132031. [CrossRef]

110. Kumar, R.; Al-Dossary, O.; Kumar, G.; Umar, A. Zinc Oxide Nanostructures for NO_2 Gas–Sensor Applications: A Review. *Nanomicro Lett.* **2015**, *7*, 97–120. [CrossRef]
111. Jung, G.; Ju, S.; Choi, K.; Kim, J.; Hong, S.; Park, J.; Shin, W.; Jeong, Y.; Han, S.; Choi, W.Y.; et al. Reconfigurable Manipulation of Oxygen Content on Metal Oxide Surfaces and Applications to Gas Sensing. *ACS Nano* **2023**, *17*, 17790–17798. [CrossRef] [PubMed]
112. Lu, N.; Zhang, M.; Ding, L.; Zheng, J.; Zeng, C.; Wen, Y.; Liu, G.; Aldalbahi, A.; Shi, J.; Song, S.; et al. Yolk–Shell Nanostructured Fe_3O_4@C Magnetic Nanoparticles with Enhanced Peroxidase-like Activity for Label-Free Colorimetric Detection of H_2O_2 and Glucose. *Nanoscale* **2017**, *9*, 4508–4515. [CrossRef] [PubMed]
113. Sun, C.; Duan, Z.; Wang, P.; Zhang, X.; Huang, M.; Cao, F.; Lin, W.; Wang, H.; Chen, Y.; Shi, X.-R. Modulation of Graphene and Graphdiyne by $Metal_n$ (n = 1–5) Adsorption and Nucleation and the Effect on Hydrogen Evolution Reaction. *Appl. Surf. Sci.* **2022**, *580*, 152197. [CrossRef]
114. Hyodo, T.; Okusa, T.; Sakata, W.; Ueda, T.; Shimizu, Y. Impacts of Surface Modification of Pt-Sensing Electrodes with Au on Hydrogen-Sensing Properties and Mechanism of Diode-Type Gas Sensors Based on Anodized Titania. *ACS Sens.* **2023**, *8*, 61–70. [CrossRef] [PubMed]
115. Liu, R.; Shi, X.-R.; Wen, Y.; Shao, X.; Su, C.; Hu, J.; Xu, S. Trimetallic Synergistic Optimization of 0D NiCoFe-P QDs Anchoring on 2D Porous Carbon for Efficient Electrocatalysis and High-Energy Supercapacitor. *J. Energy Chem.* **2022**, *74*, 149–158. [CrossRef]
116. Xu, S.; Liu, R.; Shi, X.; Ma, Y.; Hong, M.; Chen, X.; Wang, T.; Li, F.; Hu, N.; Yang, Z. A Dual CoNi MOF Nanosheet/Nanotube Assembled on Carbon Cloth for High Performance Hybrid Supercapacitors. *Electrochim. Acta* **2020**, *342*, 136124. [CrossRef]
117. Liu, R.; Xu, S.; Shao, X.; Wen, Y.; Shi, X.; Huang, L.; Hong, M.; Hu, J.; Yang, Z. Defect-Engineered NiCo-S Composite as a Bifunctional Electrode for High-Performance Supercapacitor and Electrocatalysis. *ACS Appl. Mater. Interfaces* **2021**, *13*, 47717–47727. [CrossRef]
118. Bell, J.G.; Huangfu, S.; Artiglia, L.; Graule, T.; Stuer, M. Hydrogen Spillover Drives Room Temperature Sensing on Spark Plasma Sintered $BaTiO_3$ with Pt Electrodes. *J. Mater. Chem. A Mater.* **2024**, *12*, 31993–32013. [CrossRef]
119. Zhang, R.; Lu, N.; Zhang, J.; Yan, R.; Li, J.; Wang, L.; Wang, N.; Lv, M.; Zhang, M. Ultrasensitive Aptamer-Based Protein Assays Based on One-Dimensional Core-Shell Nanozymes. *Biosens. Bioelectron.* **2020**, *150*, 111881. [CrossRef]
120. Cui, T.; Li, D.; Hirtz, T.; Xu, J.; Qiao, Y.; Xu, H.; Tian, H.; Liu, H.; Yang, Y.; Ren, T.-L. Graphene-Based Sensors for Human-Machine Interaction. *Carbon Future* **2024**, *1*, 9200005. [CrossRef]
121. Ferko, N.; Djeziri, M.A.; Al Sheikh, H.; Moubayed, N.; Bendahan, M.; El Rafei, M.; Seguin, J.L. Methodology for Estimating Ethanol Concentration with Artificial Intelligence in the Presence of Interfering Gases and Measurement Delay. *Sens. Actuators B-Chem.* **2024**, *421*, 136502. [CrossRef]
122. Li, J.W.; Weng, H.D.; Yang, Q.Q.; Shen, J. Data-Driven Diagnosis Method of High-Pressure Hydrogen Leakage Based on Actual Driving Conditions and Probabilistic Neutral Network. *Int. J. Hydrogen Energy* **2024**, *71*, 411–421. [CrossRef]
123. Shao, S.F.; Yan, L.W.; Zhang, L.; Zhang, J.; Li, Z.X.; Kim, H.W.; Kim, S.S. Utilizing Data Mining for the Synthesis of Functionalized Tungsten Oxide with Enhanced Oxygen Vacancies for Highly Sensitive Detection of Triethylamine. *ACS Appl. Mater. Interfaces* **2024**, *16*, 6098–6112. [CrossRef]
124. Nakano-Baker, O.; Fong, H.; Shukla, S.; Lee, R.V.; Cai, L.; Godin, D.; Hennig, T.; Rath, S.; Novosselov, I.; Dogan, S.; et al. Data-Driven Design of a Multiplexed, Peptide-Sensitized Transistor to Detect Breath VOC Markers of COVID-19. *Biosens. Bioelectron.* **2023**, *229*, 115237. [CrossRef] [PubMed]
125. Yang, R.X.; McCandler, C.A.; Andriuc, O.; Siron, M.; Woods-Robinson, R.; Horton, M.K.; Persson, K.A. Big Data in a Nano World: A Review on Computational, Data-Driven Design of Nanomaterials Structures, Properties, and Synthesis. *ACS Nano* **2022**, *16*, 19873–19891. [CrossRef] [PubMed]